OPTIMAL DESIGN OF PHOTONIC CRYSTALS

MEN HAN

(*B.Eng., NUS,*

S.M., MIT,

S.M., NUS)

A THESIS SUBMITTED

FOR THE DEGREE OF DOCTOR OF PHILOSOPHY

IN COMPUTATIONAL ENGINEERING

SINGAPORE-MIT ALLIANCE

NATIONAL UNIVERSITY OF SINGAPORE

2011

Acknowledgments

Throughout the course of this doctoral research, many great minds and kind souls have been part of the influencing and shaping force. This has been a most memorable journey filled with their wisdom, advice and friendship.

My deepest gratitude goes to Professor Jaime Peraire, a truly illuminating advisor and a tremendous source of inspiration, motivation and guidance. Ever since our first encounter at a faculty-student meeting in Singapore back in my college senior year in 2005, I have always been fascinated by Jaime's brilliant scientific ideas, his unstoppable energy and captivating humor. I am very grateful for his supportive and inspirational mentoring style, which has fostered me to become more independent and self-initiative.

My equally sincere gratitude goes to Professor Lim Kian Men. He has been the most understanding and accommodating advisor, under whom I was granted tremendous trust to explore and experiment freely. At the same time, he is always available to provide any help and advice when needed which I deeply respect and appreciate.

I would like to thank my thesis committee members. Professor Toh Kim Chuan has been one of my deeply revered professors, not only because of his kind and helpful advice, but also for his efficient and remarkably (almost) bug-free "SDPT3" solver that has made my life so much easier. Professor Karen Willcox has never been shy to share with me her personal experiences and timely give me the much-needed encouragement. She has always inspired me with her perseverant willpower and ingenuous personality. For that, I consider Karen my role model. I am also very grateful to all my thesis committee members as well as advisors for being accommodating to overcome the time difference, which has allowed me to receive constant advice via video conferences until finally defend this work.

I would also like to thank my collaborators with whom two journal papers have been published on this project. Doctor Ngoc-Cuong Nguyen is in fact more than a collaborator, he has been my closest and most respectable mentor for the past five years. I do not think I could have learned and grown so much as

a researcher if it had been for his constant encouragement and endless advice. His own dedication to research and the rewarding accomplishments have greatly inspired me to follow in his footsteps closely. Professor Robert Freund is anther one of the professors that I constantly look up and revere. I commend him for his respectable work ethics and thank him for his unwearied guidance. Great appreciation goes to Professor Pablo Parillo for his flashes of genius that have enabled us to overcome many obstacles in this research. Special thanks go to Professor Steven Johnson for his most generous advice and helpful suggestions that have enlightened me.

Numerous staff in SMA offices from both Singapore and MIT have lent a helpful hand. I would like to thank, Jason Chong for working on a tight schedule to make the oral defense happen on time, as well as Juliana and Neo for their timely assistance. Thanks to Jocelyn Sales and Doctor John Desforge for the tender loving care they promised even before the start of my doctoral study. They have made my journey with SMA so warm, fun and memorable. Jean from ACDL and Laura from CDO have been nothing short of kindness, they have painted beautiful colors to my cold Boston days.

I would like to extend a warm thank you to all my friends who have been helpful and supportive throughout the journey of my doctoral study. The precious moments we shared across the kitchen counters, over the dinner tables, at celebratory parties and gatherings, have not only helped me keep my sanity after the long days of work, but have also been an immensely enjoyable part of my life. In no particular order, many thanks go to, Chewhooi, Haiying and WW, Christina, Sunwei, Julei, Josephine, Shann, Zhoupeng, Ruxandra, Smaranda, Alex, Thanh, and Vanbo.

Finally, none of this could have been possible without the unwavering love and care of my family. My parents have been the best parents a child can ever have. They have always supported every dream I wish to pursue and created a wonderful and comforting life for me to completely immerse myself in. Their unconditional love and constant faith have never been absent despite the distance. To them, I give my heart-felt gratitude.

The most special thank-yous go to my fiance, Bogdan Fedeles, who has been

a constant source of love, inspiration and strength all these years. I am deeply grateful for his passion and appreciation, for his patience and tolerance, for his encouragement and support. Bogdan is also my best friend in life, with whom I can have engaging conversations on myriad topics, with whom I can play a competitive board game or tennis match, with whom I can enjoy a home-cooked dinner or a relaxing movie, with whom I can have a whole lifetime of happiness. Thank you, Bogdan, for being my life and for loving me.

To my family, I dedicate this thesis.

Contents

Summary

The present work considers the optimal design of photonic crystals. Convex optimization will be formally used for the purpose of designing photonic crystal devices with desired eigenband structures. In particular, two types of devices will be studied. The first type is a "two-dimensional" photonic crystal with discrete translational symmetry in the transverse plane, and is invariant along the longitudinal direction. The desired band structure of this device is one with optimal band gap between two consecutive eigenmodes. The second type is a three-dimensional photonic crystal fiber, which can be constructed schematically from the first type of device by introducing a defect in the transverse plane and breaking the translational symmetry. The desired feature of this device is to possess a band structure with an optimal band width at a certain propagation constant. The two design problems are analogous in that the difference between two consecutive eigenmodes is the objective function, and the disparity lies in the evaluation of eigenvalues with respect to different sets of wave vectors.

The mathematical formulations of both optimization problems lead to an infinite-dimensional Hermitian eigenvalue optimization problem parameterized by the dielectric function. To make the problem tractable, the original eigenvalue problem is discretized using the finite element method into a series of finite-dimensional eigenvalue problems for appropriate values of the wave vector parameter. The resulting optimization problem is large-scale and non-convex, with low regularity and a non-differentiable objective. By restricting to appropriate sub-eigenspaces, and employing mesh adaptivity, we reduce the large-scale non-convex optimization problem via reparametrization to a sequence of small-scale convex semidefinite programs (SDPs) for which modern SDP solvers can be efficiently applied.

We present comprehensive optimal structures of photonic crystals of different lattice types with numerous single and multiple, absolute and complete optimal band gaps, as well as single-mode single-polarization photonic crystal fiber structures of different lattice types with optimal band width for which only single guided mode can propagate.

The optimized structures exhibit patterns which go far beyond typical physical intuition on periodic media design.

List of Tables

List of Figures

Chapter 1

Introduction

1.1 Background

1.1.1 Photonic crystals

Photonic crystals will grant us the control of light. When *properly* designed, these structures, comprised of periodically arranged electromagnetic media, can exhibit certain periodic potentials to the electromagnetic waves and affect their propagation through it. Such fine control on light propagation has attracted considerable interest in recent years, as photonic crystals have proven very important as device components for integrated optics, including frequency filters[26], waveguides[25], switches[53], and optical buffers[63].

From the microscopic point of view, a crystal is a periodic arrangement of atoms or molecules. Such a pattern (or *lattice*) presents a periodic potential to electrons traveling though it. Quantum mechanics explains the flow of electrons in such a periodic potential as propagation of waves. Thus the electrons can propagate through the bulk without being scattered by the constituents of the crystal.

The photonic crystal is an optical analogue of the periodic media, in which the periodic arrangements of atoms and molecules are replaced with layers of alternating dielectric materials, see Figure 1.1. The periodic dielectric material can produce many of the same phenomena for photons that the periodic atomic potential has on electrons. In particular, one can construct a photonic crystal with a *photonic band gap*, preventing light with certain frequencies from

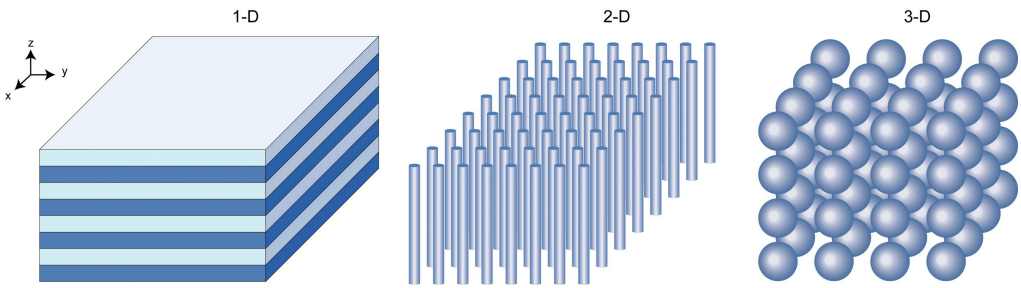

Figure 1.1: Schematic examples of one-, two-, and three-dimensional photonic crystals. The dimensionality of a photonic crystal is defined by the periodicity of the dielectric materials along one or more axes.

propagating in certain directions. Moreover, photonic crystals can channel propagation of light in more effective ways than homogeneous dielectric media, such as *index guiding* in photonic crystal fibers.

Band gap

A band gap is a range of frequency ω in which the propagation of electromagnetic waves (EM waves) at certain wave vector(s) is prohibited, and is sandwiched in between propagating states. According to the range of prohibitive wave vectors and polarizations, band gaps can be classified into three types. *Incomplete band gaps* are that which exist over a subset of all possible propagating wave vectors and polarizations; *Absolute band gaps*(ABG) are defined when the propagation is blocked for all possible wave vectors of a specific polarization; Lastly, *complete band gaps*(CBG) are that in which no propagation is allowed for any polarizations at any wave vectors.

The photonic crystal's periodic distribution of dielectric materials affects the propagation of electromagnetic waves in the same way as the periodic potential of a semiconductor affects the motion of electrons. In essence, the low-frequency modes concentrate their energy in the high-ε regions, where ε is used throughout this work to denote the dielectric constant, while high-frequency modes tend to concentrate their energy in the low-ε regions. The *band gap* phenomenon is a consequence of the localization of the low-frequency and high frequency oscillating EM waves, where the periodic differences exist in ε. Many of the promising applications of two- and three-dimensional photonic crystals to date are based on the locations and sizes of those band gaps [25, 26]. For example, a photonic

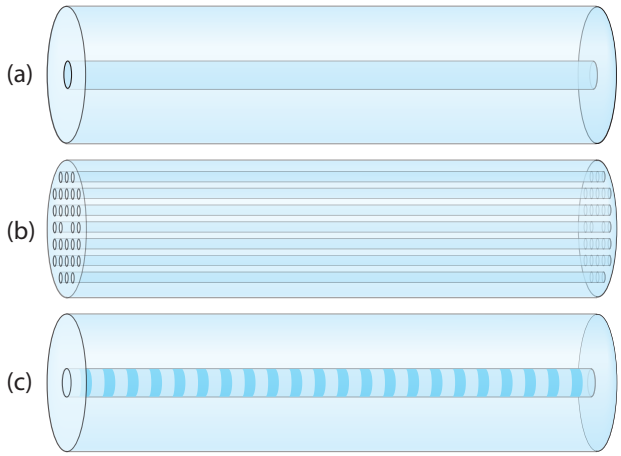

Figure 1.2: [Schematic illustrations of various waveguide operating with the index guiding mechanism. (a) Conventional fiber with step-index profile; (b) Photonic crystal holey fiber; (c) Fiber Bragg gratings.

crystal with a band gap can be used as *band filter* by rejecting frequencies within the gap; a photonic crystal with a band gap can also be carved into a *resonant cavity*, in which the walls are designed to reflect the frequencies within the gap.

Index guiding

Index guiding (or *total internal reflection*) is a confinement mechanism in which electromagnetic waves (in particular, EM waves in the visible frequency range, light) are confined within a *waveguide* consisting of *core* regions with a higher effective refractive index (or higher permittivity), surrounded by *cladding* regions with lower effective refractive index. A wide variety of dielectric waveguides can operate with such a mechanism. Among those, we find conventional fibers with a step-index profile, photonic crystal "holey" fibers where a two-dimensional photonic crystal is used as cladding with a core of higher effective refractive index that breaks the periodicity over the cross-section, and fiber Bragg gratings with a periodic grating along fiber's propagation direction, shown in Figure 1.2. It is not of our interest in this work to consider other guiding mechanisms such as photonic band gaps of photonic crystal fibers or metallic waveguides.

A photonic crystal fiber (PCF) that employs the index guiding mechanism for light confinement can typically be engineered by filling up one or several holes of a two-dimensional periodic photonic crystal. Thus, a much higher dielectric contrast between the solid core and holey cladding can be obtained than with

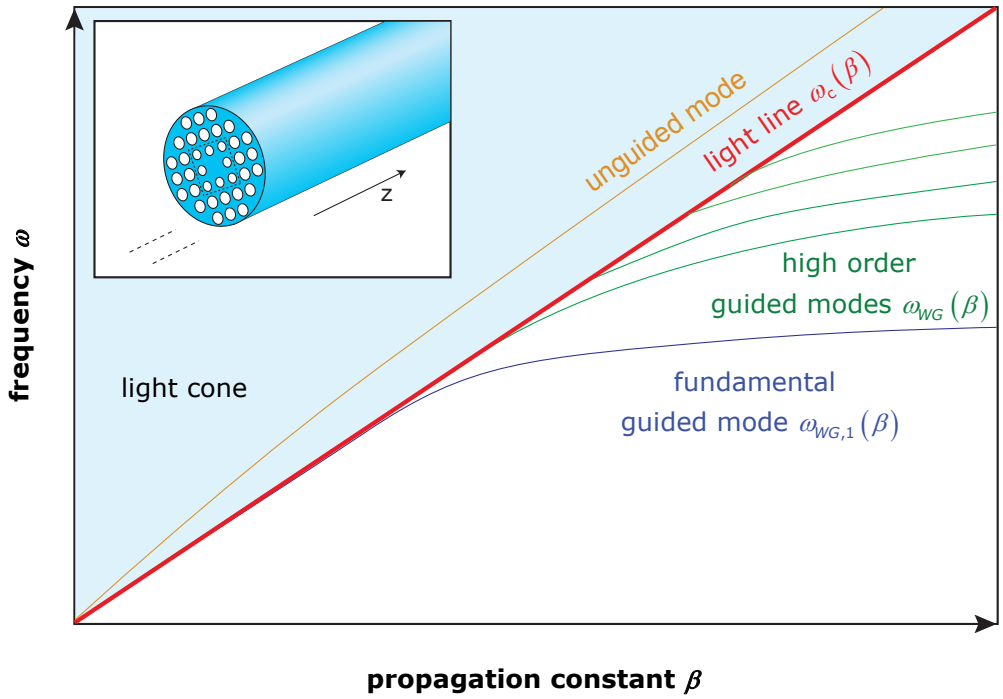

Figure 1.3: Example of dispersion relation of a photonic crystal fiber, showing the light cone shaded in light blue, the light line $\omega_c(\beta)$, the fundamental guided mode $\omega_{WG,1}$, the higher-order guided modes, and an unguided mode above the light line.

conventional solid fiber materials, which is a means of creating some unusual dispersion relations, shown in Figure 1.3. In the absence of the core, all the non-localized modes propagating in the infinite periodic cladding form the *light cone* that includes all the permissible modes for propagation. The minimum frequency ω_c at each propagation constant β that defines the lower boundary of the light cone is called *light line*, or *fundamental space-filling mode (FSM)*. Outside of the light cone, i.e., below the light line, only evanescent modes that decay exponentially in the transverse directions can exist in the cladding. If a core with a higher "average" index is introduced in this design, one or more modes will be pulled beneath the light line to have frequencies $\omega < \omega_c$. These modes will very likely be localized inside the core and decay exponentially into the cladding far from the core. The further they are below the light line, the faster the decay. These are called *index-guided modes*. Figure 1.4 demonstrates the field profiles of a localized and a non-localized mode.

In an ordinary index-guided waveguide, as the frequency ω goes higher, more

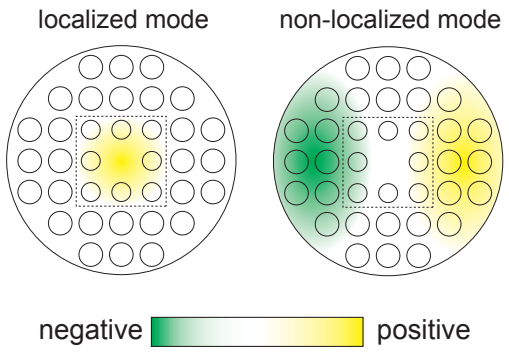

Figure 1.4: Field profiles of localized and non-localized modes. The dashed box indicates the core of the fiber, while the cladding consists of the surrounding photonic crystals. A localized mode has a compact support within the fiber cross section, i.e., decaying exponentially outside of the core into the cladding, and a non-localized mode does not.

modes will be pulled below the light line to become guided modes. However, as first pointed out in [11], photonic crystal fibers can remain endlessly single-mode. The phenomenon can be explained by the fact that the reduced index contrast between core and cladding at smaller wavelengths leads to a weaker confinement strength, and thus the higher-order guided modes will remain above the light line. Due to the common cylindrical cross-sectional shape of the fibers, the so-called single-mode is actually composed of two doubly degenerate modes corresponding to two polarizations. A variation of the single-mode waveguide called *single polarization single mode (SPSM)* is a truly single-mode waveguide because it supports a single guided mode solution. In an SPSM fiber, only one linearly polarized mode is guided while the mode with orthogonal polarization is suppressed. In contrast, a birefringent fiber has two guided polarizations, but travel at different speeds. Such waveguides are important as polarization-maintaining fibers [45]. The notion of *band width*, similar to the band gap discussed before, is defined as a range of frequency at certain wave vector(s) in which only a single guided mode exists.

1.1.2 Optimal design

The optimal conditions for the appearance of photonic band gaps were first studied for one-dimensional crystals by Lord Rayleigh in 1887 [48]. A one dimensional photonic crystal consists of alternating layers of material with different dielectric

constants (e.g., a quarter-wave stack). An incident light of proper wavelength can be completely reflected by being partially reflected at each layer interface and destructively interfering to eliminate the forward propagation. This phenomenon is also the basis of many higher dimensional devices. In the one-dimensional periodic structure, the band gap can be widened by increasing the contrast in the refractive index and the difference in width between the materials. Furthermore, it is possible to create band gaps for any particular frequency by changing the periodicity length of the crystal. Unfortunately, in two or three dimensions one can only suggest rules of thumb for the existence of a band gap in a periodic structure, since no rigorous criteria have yet been determined. Thus the design of two- or three-dimensional crystals has largely been a trial and error process, which is far from optimal. Indeed, the possibility of two- and three-dimensionally periodic crystals with corresponding two- and three-dimensional band gaps was only suggested in 1987 by Yablonovitch [60] and John [30], 100 years after Rayleigh's discovery of photonic band gap in one dimension, .

From a mathematical viewpoint, the calculation of the band gap reduces to the solution of an infinite-dimensional Hermitian eigenvalue problem parameterized by the dielectric function and the wave vector. In the design setting, however, the central question is: which periodic structures, composed of arbitrary arrangements of two or more different materials, produce the largest band gaps around a certain frequency? This question can be rigorously addressed by formulating an optimization problem for the parameters that represent the material properties and geometry of the periodic structure. The resulting problem is infinite-dimensional with an infinite number of constraints. After appropriate discretization in space and consideration of a finite set of wave vectors, a large-scale finite-dimensional eigenvalue problem is obtained; this problem is non-convex and is known to be non-differentiable when eigenvalue multiplicities exist. The current state-of-the-art work done on this problem falls into two broad categories. The first approach tries to find the "optimal" band structure by parameter studies — based on prescribed inclusion shapes (e.g., circular or hexagonal inclusions) [24], fixed topology [62], or geometric considerations from the interpretation of an extensive numerical optimization study [50]. The second

approach attempts to use formal topology optimization techniques [16, 20, 51], and level set method [33], which allow for more flexible geometrical representations, and result in diverse optimal crystal structures. Nevertheless, both approaches typically use gradient-based optimization methods. While these methods are attractive and have been quite successful in practice, the optimization processes employed explicitly compute the sensitivities of eigenvalues with respect to the dielectric design function, which are local sub-gradients for such a non-differentiable problem. Consequently, gradient-based solution methods often suffer from the lack of regularity of the underlying problem when eigenvalue multiplicities are present, as they typically are at or near the solution.

Besides the early studied band gap optimization problems, photonic crystals have gained popularity in many other applications [53, 63]. The single polarization single mode photonic crystal fiber mentioned above is among one of them. For these devices, the calculation of the operating band width according to the dispersion relations similarly reduces to finding the solution of an infinite-dimensional Hermitian eigenvalue problem. The design of the photonic crystal fiber that supports only one guided mode of a single polarization with optimal band width can also be mathematically formulated to the control of dispersion relations that are parameterized by the dielectric function. To our best knowledge, the optimal design of such a device to date has been strictly limited to the study of simple geometric parametrization. More precisely, these studies only investigated photonic crystal fibers with a fixed cladding pattern but variable core composition of prescribed inclusion shapes. In most work, the authors construct the cross section of photonic crystal fiber with a fixed cladding pattern, and allowed the central core to vary (design region of the optimization) with prescribed topology, e.g., one central filled air hole, and four or eight enlarged holes arranged in two rows above and below the central filled hole in a triangular lattice [49]; or six enlarged holes arranged in two rows in a rectangular lattice [64]; or two enlarged holes arranged to the left and right of the filled hole [32]. Some more elaborate core compositions consist of both enlarged and shrunk air holes [4]. The obvious drawback of such studies is the rigid topology of the fiber cross sections consequently, compared with those obtained using formal topology

optimization methods.

If one were to design such a device possessing optimal operating band width by employing topological methods which allow for maximum geometrical variations, followed by gradient-based methods for optimization, the reliable computation of eigenvalue sensitivities would become extremely challenging due to the high density state of the eigenvalues. While these gradient methods perform well in the published works on photonic crystal band gap optimization problems, in which the eigenvalue degeneracy is mainly an accidental artifact of the artificial periodicity chosen for the wave vectors in the Brillouin zone [29], they fail to make progress in the band width problem in which the eigenvalue degeneracies are physically prevalent.

1.2 Scope

1.2.1 Thesis contributions

The central theme of the work in this thesis is the optimal design of photonic crystal using convex optimization. We propose a new approach based on semidefinite programming (SDP) and subspace methods for the optimal design of photonic band structure. In the last two decades, SDP has emerged as the most important class of models in convex optimization, [1, 3, 46, 57, 59]. SDP encompasses a huge array of convex problems as special cases, and is computationally tractable (usually comparable to least-square problems of comparable dimensions). There are three distinct properties that make SDP well suited to the band structure optimization problem. First, the underlying differential operator is Hermitian and positive semidefinite. Second, the objective and associated constraints involve bounds on eigenvalues of matrices. And third, as explained in this thesis, the original non-convex optimization problem can be approximated by a semidefinite program for which SDP can be well applied, thanks to the its efficiency and robustness of handling this type of spectral objective and constraints.

The optimal design problems for both band gap and band width in the respective photonic crystal devices are analogous in that the difference between two consecutive eigenmodes is the objective function, and the disparity lies in

the evaluation of eigenvalues with respect to different sets of wave vectors. In our optimization approach, we first reformulate the original problem of maximizing the difference between eigenvalues as an optimization problem in which we optimize the distance in eigenvalues between two orthogonal subspaces. The first eigenspace consists of eigenfunctions corresponding to the lower eigenvalues, whereas the second eigenspace consists of eigenfunctions of higher eigenvalues. In this way, the eigenvalues are no longer present in our formulation; however, like the original problem, the exactly reformulated optimization problem is large-scale. To reduce the problem size, we truncate the high-dimensional subspaces to only a few eigenfunctions below and above the band gap [17, 47], thereby obtaining a new small-scale yet non-convex optimization problem. Finally, we keep the subspaces fixed at a given decision parameter vector and use a reparametrization of the decision variables whenever necessary to obtain a convex semidefinite optimization problem for which SDP solution methods can be effectively applied. We apply this approach to optimize various band gaps in two-dimensional photonic crystals, and also optimize the band width in designing SPSM PCF.

By analyzing the initial optimal photonic crystal structures which consist of two dielectric materials, we realize that a non-uniform computation mesh with low resolution in the regions of uniform material properties and high resolution at the material interface can lead to lower degrees of freedoms and fewer optimization decision variables, hence a more efficient band structure computation and optimization. Adaptive mesh refinement techniques have been widely used to reduce the computation cost and improve computation efficiency associated with the numerical solution of partial differential equations [19, 7]. Since our computational technique are based on the finite element method, mesh refinement can be easily incorporated. In our improved approach, we start the optimization with a relatively coarse mesh, converge to a near-optimal solution, and subdivide only chosen elements of the finite element mesh based on judiciously devised refinement criteria. The optimization is then restarted with this near-optimal solution extrapolated on the refined mesh as the initial configuration. The mesh adaptivity approach is incorporated into the optimization procedure to achieve reduced computation cost and enhanced efficiency.

A detailed assessment of the computational efficiency of the proposed approach compared to alternative methods is outside the scope of this thesis. We note that the performance of the methods that require sensitivity information of the eigenvalues with respect to the dielectric function will deteriorate when eigenvalue multiplicities occur. However, our approach is designed to deal with such situations and therefore, we expect it will perform with increased robustness in complex realistic applications.

1.2.2 Thesis outline

The necessary physical and mathematical background is reviewed in chapter 2. These fundamental concepts will be frequently used throughout the thesis. In chapter 3, two physical problems are introduced, the two-dimensional photonic crystal and the three-dimensional photonic crystal fiber. Mathematical formulations and finite element method based solution methods are derived to solve the corresponding eigenvalue equations for the frequency and field variables of the electromagnetic waves in each case. Chapter 3 also covers the mesh adaptivity methods for both problems to demonstrate the reliable computation of the eigenvalues. Having established the computation procedure for the eigenvalues (or frequencies of the electromagnetic waves), we discuss in chapter 4 the *band gap optimization* problem – the most important and often studied optimal design problem of photonic crystals. Using subspace approximation and reduction and SDP relaxation, we propose a *convex formulation* of the original nonlinear, nonconvex problem. Adaptive mesh refinement is also seamlessly incorporated into the algorithm to improve the computational efficiency. Extensive optimal designs of the two-dimensional photonic crystals are presented with optimal band gaps of various configurations, e.g., absolute band gaps, complete band gaps, and multiple band gap. In chapter 5, we study the *band width optimization* problem arising in the photonic crystal fiber, and investigate the design of the single-mode single polarization fibers with several formal convex optimization formulations. We will demonstrate that the optimization recipes developed for the band gap optimization problem can be extended to this similar yet more complicated physical problem. The resulting optimal crystal structures as well

as validation of the field variable intensities will be presented. Finally in chapter 6, we summarize our findings and discuss the future implications of our work.

Chapter 2

Building Blocks

This chapter serves to review the necessary physical and mathematical concepts that will be frequently used throughout the thesis. We will first review electromagnetism in dielectric media, which introduces the physics of the light propagation in photonic crystals. Functional analysis will be briefly reviewed next, which proves useful in understanding the finite element method that will be reviewed afterwards. Finally, we review the convex optimization which will turn out to be the fundamental optimization tool of our design algorithm.

2.1 Review of Electromagnetism in Dielectric Media

The propagation of electromagnetic waves in dielectric media is governed by Maxwell equations.

2.1.1 Maxwell equations

Macroscopic equations

With appropriate assumptions in place [28, 29], the macroscopic Maxwell equations governing the electromagnetism in a mix dielectric medium without source can be written as,

$$\begin{aligned} \nabla \cdot \boldsymbol{H}(\boldsymbol{r},t) = 0, \qquad & \nabla \times \boldsymbol{E}(\boldsymbol{r},t) + \mu_0 \tfrac{\partial \boldsymbol{H}(\boldsymbol{r},t)}{\partial t} = 0, \\ \nabla \cdot [\varepsilon(\boldsymbol{r})\boldsymbol{E}(\boldsymbol{r},t)] = 0, \quad & \nabla \times \boldsymbol{H}(\boldsymbol{r},t) - \varepsilon_0 \varepsilon(\boldsymbol{r}) \tfrac{\partial \boldsymbol{E}(\boldsymbol{r},t)}{\partial t} = 0, \end{aligned} \tag{2.1}$$

where $\boldsymbol{E}$ and $\boldsymbol{H}$ are the macroscopic electric and magnetic fields respectively. They are both functions of the Cartesian position vector $\boldsymbol{r}$ and vary with time t. $\varepsilon_0 \approx 8.854\times10^{-12}$Farad/meter is the vacuum permittivity; $\varepsilon(\boldsymbol{r})$ is a scalar dielectric function, also called relative permittivity. The explicit frequency dependence (material dispersion) of $\varepsilon(\boldsymbol{r})$ can be appropriately ignored[1] and is assumed to be purely real and positive. $\mu_0 = 4\pi \times 10^{-7}$Henry/meter is the vacuum permeability; $\mu(\boldsymbol{r})$, the relative magnetic permeability, is very close to unity for most dielectric materials of interest, therefore it does not appear in the equations (2.1). As a result, $\varepsilon = n^2$, n being the refractive index from Snell's law. ($\varepsilon\mu = n^2$ in general.)

Eigenvalue problem

Due to the linearity of the Maxwell equations, the temporal and spatial dependence of both $\boldsymbol{E}$ and $\boldsymbol{H}$ fields can be separated by expanding the fields into a series of harmonic modes. The standard trick is to write the harmonic mode as the product of the spatial mode profile and a temporal complex exponential: $\boldsymbol{E}(\boldsymbol{r},t) = \boldsymbol{E}(\boldsymbol{r})e^{-i\omega t}$, and $\boldsymbol{H}(\boldsymbol{r},t) = \boldsymbol{H}(\boldsymbol{r})e^{-i\omega t}$. Inserting these into equations (2.1), we obtain the two divergence equations:

$$\nabla \cdot \boldsymbol{H}(\boldsymbol{r}) = 0, \qquad \nabla \cdot (\varepsilon(\boldsymbol{r})\boldsymbol{E}(\boldsymbol{r})) = 0, \tag{2.2}$$

which ensure that the displacement ($\boldsymbol{D}(\boldsymbol{r}) = \varepsilon_0\varepsilon(\boldsymbol{r})\boldsymbol{E}(\boldsymbol{r})$) and the magnetic fields are built up of *transverse* electromagnetic waves. That is, equations (2.2) require $\boldsymbol{a}\cdot\boldsymbol{k} = 0$ for a plane wave $\boldsymbol{H}(\boldsymbol{r}) = \boldsymbol{a}e^{i\boldsymbol{k}\cdot\boldsymbol{r}}$ of some wave vector $\boldsymbol{k}$. The simple physical interpretation is that there is no point sources or sinks of displacement or magnetic fields in the medium. The two curl equations in (2.1) couple the electric and magnetic fields together in the form of

$$\nabla \times \boldsymbol{E}(\boldsymbol{r}) - i\omega\mu_0\boldsymbol{H}(\boldsymbol{r}) = 0, \qquad \nabla \times \boldsymbol{H}(\boldsymbol{r}) + i\omega\varepsilon_0\varepsilon(\boldsymbol{r})\boldsymbol{E}(\boldsymbol{r}) = 0. \tag{2.3}$$

[1] Instead, the value of the dielectric constant is chosen appropriately to the frequency range of the physical system being considered .[29]

To decouple these two quantities, one can divide the second equation by $\varepsilon(\boldsymbol{r})$, take the curl, then eliminate $\nabla \times \boldsymbol{E}$ using the first equation. This yields our *master equation* only in $\boldsymbol{H}(\boldsymbol{r})$

$$\nabla \times \left(\frac{1}{\varepsilon(\boldsymbol{r})} \nabla \times \boldsymbol{H}(\boldsymbol{r}) \right) = \left(\frac{\omega}{c} \right)^2 \boldsymbol{H}(\boldsymbol{r}), \qquad \text{in } \mathbb{R}^d. \tag{2.4}$$

Similarly, one can obtain another equation only in $\boldsymbol{E}(\boldsymbol{r})$

$$\frac{1}{\varepsilon(\boldsymbol{r})} \nabla \times (\nabla \times \boldsymbol{E}(\boldsymbol{r})) = \left(\frac{\omega}{c} \right)^2 \boldsymbol{E}(\boldsymbol{r}), \qquad \text{in } \mathbb{R}^d, \tag{2.5}$$

where $c = 1/\sqrt{\varepsilon_0 \mu_0}$ is the speed of light in vacuum. In practice, we only need to solve one of the equation (2.4) or (2.5) together with the transversality constraint (2.2) on the field being computed, and then we can recover the other quantity via (2.3). The transversality constraint for the latter quantity is automatically ensured because the divergence of a curl is always zero.

Scaling properties

The linear Hermitian eigenvalue problem of our master equation in (2.4) has no fundamental constant on the dimensions of length; moreover, there is also no fundamental value of the dielectric constant. In other words, the master equation is *scale invariant*. We first examine the contraction or expansion of the distance. Let us start with an eigenmode $\boldsymbol{H}(\boldsymbol{r})$ of corresponding frequency ω in a dielectric medium represented by $\varepsilon(\boldsymbol{r})$. Assume the dielectric configuration is scaled by a scale parameter s, and it is now expressed as $\varepsilon'(\boldsymbol{r}) = \varepsilon(\boldsymbol{r}/s)$. If we introduce in equation (2.4) the change of variables, $\boldsymbol{r}' = s\boldsymbol{r}$ and $\nabla' = \nabla/s$, and rearrange the terms,

$$\nabla' \times \left(\frac{1}{\varepsilon'(\boldsymbol{r}')} \nabla' \times \boldsymbol{H}(\boldsymbol{r}'/s) \right) = \left(\frac{\omega}{cs} \right)^2 \boldsymbol{H}(\boldsymbol{r}'/s), \tag{2.6}$$

we obtained the master equation (2.6) with a different frequency $\omega' = \omega/s$ and mode profile $\boldsymbol{H}'(\boldsymbol{r}') = \boldsymbol{H}(\boldsymbol{r}'/s)$ that can be viewed as a rescaled version of the original.

If the configuration of the dielectric function is fixed, but the value differs by

a constant factor everywhere, i.e., $\varepsilon'(\boldsymbol{r}) = \varepsilon(\boldsymbol{r})/s$, we can substitute $s\varepsilon'(\boldsymbol{r})$ into 2.4 to obtain

$$\nabla \times \left(\frac{1}{\varepsilon'(\boldsymbol{r})} \nabla \times \boldsymbol{H}(\boldsymbol{r}) \right) = s \left(\frac{\omega}{c} \right)^2 \boldsymbol{H}(\boldsymbol{r}). \tag{2.7}$$

The frequency of the new system is scaled by $\sqrt{s}$ while the mode profile $\boldsymbol{H}(\boldsymbol{r})$ remains unchanged. Based on (2.6) and (2.7), we can conclude that any coordinate transformation can be offset simply by a change of ε to keep the frequency ω intact. This powerful conceptual tool gives us extensive flexibility with a dielectric structure while retaining various similar electromagnetic properties.

2.1.2 Symmetries and Bloch-Floquet theorem

A photonic crystal can be defined by a periodic dielectric function $\varepsilon(\boldsymbol{r}) = \varepsilon(\boldsymbol{r}+\boldsymbol{R})$ possessing discrete translational symmetry. $\boldsymbol{R}$, known as the *lattice vector*, represents any linear combination of the *primitive lattice vectors* $\boldsymbol{a} = \{\boldsymbol{a_x}, \boldsymbol{a_y}, \boldsymbol{a_z}\}$. All the points defined by $\boldsymbol{R} = m_x \boldsymbol{a_x} + m_y \boldsymbol{a_y} + m_z \boldsymbol{a_z},\ m_x, m_y, m_z \in \mathbb{Z}$ make up the *Bravais lattice*; the primitive lattice vectors $\boldsymbol{a_x}, \boldsymbol{a_y}$ and $\boldsymbol{a_z}$ define the *primitive unit cell* of the Bravais lattice.

The *reciprocal lattice* of a Bravais lattice is a set of all vectors $\boldsymbol{G}$ that satisfy

$$e^{i\boldsymbol{G}\cdot\boldsymbol{R}} = 1.$$

This relation arises naturally when Fourier analysis is performed on such periodic functions. The primitive reciprocal lattice vectors $\boldsymbol{b} = \{\boldsymbol{b_x}, \boldsymbol{b_y}, \boldsymbol{b_z}\}$ can be determined through

$$\boldsymbol{b_x} = \frac{2\pi \boldsymbol{a_y} \times \boldsymbol{a_z}}{\boldsymbol{a_x} \cdot (\boldsymbol{a_y} \times \boldsymbol{a_z})}, \quad \boldsymbol{b_y} = \frac{2\pi \boldsymbol{a_z} \times \boldsymbol{a_x}}{\boldsymbol{a_x} \cdot (\boldsymbol{a_y} \times \boldsymbol{a_z})}, \quad \boldsymbol{b_z} = \frac{2\pi \boldsymbol{a_x} \times \boldsymbol{a_y}}{\boldsymbol{a_x} \cdot (\boldsymbol{a_y} \times \boldsymbol{a_z})}.$$

The primitive reciprocal lattice vectors $\boldsymbol{b_x}, \boldsymbol{b_y}$ and $\boldsymbol{b_z}$ define the primitive unit cell of the reciprocal lattice, also know as *Brillouin zone*.

In 1928, Felix Bloch pioneered the study of wave propagation in three-dimensionally periodic media, by unknowingly extending a one-dimensional theorem proposed by Gaston Floquet in 1883. Bloch's theorem [12, 27] states that the eigenfunction (e.g., $\boldsymbol{H}(\boldsymbol{r})$ in (2.4)) for a periodic system (e.g., the periodic

dielectric material in a photonic crystal, or the periodic potential in an atomic lattice) can be expressed as a product of a plane wave envelope function and a periodic function modulation:

$$\boldsymbol{H}(\boldsymbol{r}) = e^{i\boldsymbol{k}\cdot\boldsymbol{r}}\boldsymbol{H}_{\boldsymbol{k}}(\boldsymbol{r}). \tag{2.8}$$

This form is commonly know as a *Floquet mode* [36] in mechanics or *Bloch state* [43] in solid-state physics. $\boldsymbol{k}$,a *wave vector* that lies in the Brillouin zone, is a linear combination of the primitive reciprocal lattice vectors, $\boldsymbol{k} = k_x\boldsymbol{b_x} + k_y\boldsymbol{b_y} + k_z\boldsymbol{b_z}$. $\boldsymbol{H}_{\boldsymbol{k}}(\boldsymbol{r})$ is a periodic function on the Bravais lattice: $\boldsymbol{H}_{\boldsymbol{k}}(\boldsymbol{r}) = \boldsymbol{H}_{\boldsymbol{k}}(\boldsymbol{r}+\boldsymbol{R})$. Substituting (2.8) into (2.4) yields a different Hermitian eigenproblem over the primitive cell of the Bravais lattice, denoted by Ω:

$$(\nabla + i\boldsymbol{k}) \times \left(\frac{1}{\varepsilon(\boldsymbol{r})}(\nabla + i\boldsymbol{k}) \times \boldsymbol{H}_{\boldsymbol{k}}(\boldsymbol{r})\right) = \left(\frac{\omega}{c}\right)^2 \boldsymbol{H}_{\boldsymbol{k}}(\boldsymbol{r}), \qquad \text{in } \Omega. \tag{2.9}$$

Thanks to the translational periodicity of the reciprocal lattice, one needs to solve only for the eigensolutions in the set of $\boldsymbol{k}$ within the Brillouin zone closest to the $\boldsymbol{k} = \boldsymbol{0}$ origin, a region called *first Brillouin zone*. Moreover, due to the additional symmetry of the lattice, rotation, mirror reflection, and inversion, eigenvalues ($\lambda = (\omega(\boldsymbol{k})/c)^2$)/frequencies ($\omega(\boldsymbol{k})$) computed from the first Brillouin zone wave vectors may contain redundancy with the full symmetry of the point group of the lattice [29]. Therefore, we also define the *irreducible Brillouin zone* as the smallest region within the first Brillouin zone after removing the redundancy for which $\omega(\boldsymbol{k})$ are not related by symmetry. We will illustrate examples of this approach in Chapter 3 when the eigenvalue band structure calculation is discussed.

2.2 Review of Functional Analysis

2.2.1 Function spaces

Linear vector space

A linear vector space is a set $\boldsymbol{V}$ over a field F together with two binary operations: addition, $\boldsymbol{u}, \boldsymbol{v} \in \boldsymbol{V} \rightarrow \boldsymbol{u} + \boldsymbol{v} \in \boldsymbol{V}$, and scalar multiplication, $\boldsymbol{u} \in \boldsymbol{V}, \alpha \in F \rightarrow \alpha\boldsymbol{u} \in \boldsymbol{V}$ that satisfies the following 8 axioms, $\forall \boldsymbol{u}, \boldsymbol{v}$ and $\boldsymbol{w} \in \boldsymbol{V}$, and $\alpha, \beta \in F$:

(1) Commutativity of addition: $\boldsymbol{u} + \boldsymbol{v} = \boldsymbol{v} + \boldsymbol{u}$;

(2) Associativity of addition: $\boldsymbol{u} + (\boldsymbol{v} + \boldsymbol{w}) = (\boldsymbol{u} + \boldsymbol{v}) + \boldsymbol{w}$;

(3) Identity element of addition: $\forall \boldsymbol{u} \in \boldsymbol{V}, \exists \boldsymbol{0} \in \boldsymbol{V}$, called the zero vector, such that $\boldsymbol{u} + \boldsymbol{0} = \boldsymbol{u}$;

(4) Identity element of scalar multiplication: $1\boldsymbol{u} = \boldsymbol{u}$, where $1 \in F$ denotes the multiplicative identity;

(5) Inverse elements of addition: $\forall \boldsymbol{u} \in \boldsymbol{V}, \exists -\boldsymbol{u} \in \boldsymbol{V}$, called the additive inverse of $\boldsymbol{u}$, such that $\boldsymbol{u} + (-\boldsymbol{u}) = \boldsymbol{0}$;

(6) Distributivity of scalar multiplication with respect to vector addition: $\alpha(\boldsymbol{u} + \boldsymbol{v}) = \alpha\boldsymbol{u} + \alpha\boldsymbol{v}$;

(7) Distributivity of scalar multiplication with respect to field addition: $(\alpha + \beta)\boldsymbol{u} = \alpha\boldsymbol{u} + \beta\boldsymbol{u}$;

(8) Compatibility of scalar multiplication with field multiplication: $\alpha(\beta\boldsymbol{u}) = (\alpha\beta)\boldsymbol{u}$.

Norm

A norm on a linear vector space $\boldsymbol{V}$ over a field F is a function $f : \boldsymbol{V} \rightarrow \mathbb{R}$ that satisfies the following properties, $\forall \alpha \in F$, and $\forall \boldsymbol{u}, \boldsymbol{v} \in \boldsymbol{V}$:

(1) Positive scalability: $f(\alpha\boldsymbol{u}) = |\alpha| f(\boldsymbol{u})$;

(2) Triangle inequality: $f(\boldsymbol{u} + \boldsymbol{v}) \leq f(\boldsymbol{u}) + f(\boldsymbol{v})$;

(3) Positive definiteness: $f(\boldsymbol{u}) \geq 0$, and the equality holds iff $\boldsymbol{u} = \boldsymbol{0}$.

Function f is commonly denoted as $f(\cdot) := \| \cdot \|_{\boldsymbol{V}}$. A linear vector space $\boldsymbol{V}$ together with a norm defined on itself $\| \cdot \|_{\boldsymbol{V}}$ is a normed space.

Inner product

An inner product on a linear vector space $\boldsymbol{V}$ is a map

$$(\cdot,\cdot)_{\boldsymbol{V}} := \boldsymbol{V} \times \boldsymbol{V} \to F$$

where F is the field over which the linear vector space $\boldsymbol{V}$ is defined. The inner product satisfies the following 3 axioms, $\forall \boldsymbol{u}, \boldsymbol{v}, \boldsymbol{w} \in \boldsymbol{V}$,and $\forall \alpha \in F$:

(1) Conjugate symmetry: $(\boldsymbol{u}, \boldsymbol{v})_{\boldsymbol{V}} = \overline{(\boldsymbol{v}, \boldsymbol{u})}_{\boldsymbol{V}}$;

(2) Bilinearity: $(\alpha \boldsymbol{u}, \boldsymbol{v}) = \alpha(\boldsymbol{u}, \boldsymbol{v})$; and$(\boldsymbol{u} + \boldsymbol{w}, \boldsymbol{v}) = (\boldsymbol{u}, \boldsymbol{v}) + (\boldsymbol{w}, \boldsymbol{v})$;

(3) Positive definiteness:$(\boldsymbol{u}, \boldsymbol{u}) \geq 0$, and the equality holds iff $\boldsymbol{v} = 0$.

A linear vector space $\boldsymbol{V}$ with an inner product defined on itself is a called an inner product space. One can associate a norm with every inner product as well: $\|\boldsymbol{u}\|_{\boldsymbol{V}} = (\boldsymbol{u}, \boldsymbol{u})_{\boldsymbol{V}}^{1/2}$.

Space of continuous functions

Given a non-negative integer k, we define a set of functions with continuous derivatives up to and including order k as

$$C^k(\Omega) = \{v | D^\alpha v \text{ is uniformly continuous and bounded on } \Omega, 0 \leq |\alpha| \leq k\},$$

where, for a given $\alpha \equiv (\alpha_1, \ldots, \alpha_d), \alpha_i \geq 0, 1 \leq i \leq d$,

$$D^\alpha \equiv \frac{\partial^{|\alpha|}}{\partial_{x_1}^{\alpha_1} \cdots \partial_{x_d}^{\alpha_d}}, \qquad |\alpha| = \sum_{i=1}^{d} \alpha_i.$$

If we associate $C^k(\Omega)$ with a norm defined as,

$$\|v\|_{C^k(\Omega)} = \max_{0 \leq |\alpha| \leq k} \sup_{\boldsymbol{r} \in \Omega} |D^\alpha v(\boldsymbol{r})|,$$

then $C^k(\Omega)$ is a complete normed linear space, known as *Banach space*. C_0^k is the space of continuous, kth differentiable functions with the subscript 0 indicating a compact support on Ω, i.e., vanishing on the boundary of Ω.

Lebesgue spaces

Let $p \geq 1$, the Lebesgue space, or the space of p^{th} integrable functions, $L^p(\Omega)$ is defined as

$$L^p(\Omega) \equiv \{v|\ \|v\|_{L^p(\Omega)} < \infty\},$$

where the norm is defined as,

$$\|v\|_{L^p(\Omega)} = \begin{cases} \int_\Omega |v|^p dx,\ 1 \leq p < \infty \\ \operatorname*{ess\,sup}_{x\in\Omega} |v(x)|,\ p = \infty \end{cases} \tag{2.10}$$

Note that Lebesgue spaces are also Banach spaces. Here $\int_\Omega$ denotes the Lebesgue integral. ess $\sup_{x\in\Omega} v(x)$, the essential supremum of a function $v(x)$, is defined as the greatest lower bound $C_{\max}$ of the set of all constants C, such that $|v(x)| \leq C$ "almost everywhere" on Ω, i.e., $\Omega \backslash B$ for all sets B of zero measures.

Hilbert spaces

Let k be a non-negative integer. The Hilbert space $H^k(\Omega)$ is defined as,

$$H^k(\Omega) \equiv \{v|\ D^\alpha v \in L^2(\Omega), \forall \alpha, s.t.\ |\alpha| \leq k\},$$

with associated inner product,

$$(\boldsymbol{u}, \boldsymbol{v})_{H^k(\Omega)} \equiv \sum_{|\alpha|\leq k} \int_\Omega D^\alpha \boldsymbol{u} \cdot D^\alpha \boldsymbol{v} dx,$$

and induced norm,

$$\|\boldsymbol{u}\|_{H^k(\Omega)} = \left(\sum_{|\alpha|\leq k} \int_\Omega |D^\alpha v|^2 dx \right)^{1/2}.$$

It is important to note that $L^2(\Omega)(\equiv H^0(\Omega))$ is the only Lebesgue space that is also a Hilbert space. Hilbert spaces will be used extensively in the subsequent chapters of this thesis. They are the natural generalization of Euclidean spaces in the functional setting, and thus very important for understanding the well-posedness of weak formulations and for defining the convergence rate of the finite

element method.

Sobolev spaces

Let k be a non-negative integer and $p \geq 1$. The Sobolev space $W^{k,p}(\Omega)$ is defined as,

$$W^{k,p}(\Omega) \equiv \{v | D^\alpha v \in L^p(\Omega),\ \forall \alpha, s.t. |\alpha| \leq k\}.$$

The Sobolev spaces are Banach spaces with norms defined as,

$$\|v\|_{W^{k,p}(\Omega)} \equiv \begin{cases} \left(\sum_{|\alpha|\leq k} \int_\Omega |D^\alpha v|^p dx\right)^{1/p}, & 1 \leq p < \infty, \\ \max\limits_{|\alpha|\leq k} \operatorname{ess\,sup}\limits_{x\in\Omega} |D^\alpha v(x)|, & p = \infty. \end{cases}$$

Sobolev spaces are the natural setting for the variational formulation of partial differential equations. Several cases are of particular interest. The first case is when $k = 0$, s.t., $W^{0,p}(\Omega) \equiv L^p(\Omega)$, hence the Lebesgue spaces are included in the Sobolev spaces. The second case is when $p = 2$ and it corresponds to $W^{k,2}(\Omega) \equiv H^k(\Omega)$, our earlier Hilbert spaces.

2.2.2 Linear and bilinear functionals

Linear functional

Let X be a linear space over field F. A linear transformation $\ell : X \to K$ is called a linear functional if and only if, $\forall u, v \in X$, and $\alpha, \beta \in F$,

$$\ell(\alpha u + \beta v) = \alpha \ell(u) + \beta \ell(v).$$

The set of all linear functionals on a linear space X is itself a linear space. This space, denoted by X', is called the *dual space* of X.

Bilinear functional

Let X and Y be two linear spaces over the field F. An operator $a : X \times Y \to F$ is a bilinear form if and only if, $\forall u_1, u_2 \in X, v_1, v_2 \in Y$, and $\alpha, \beta, \gamma, \lambda \in F$

$$a(\alpha u_1 + \beta u_2, \gamma v_1 + \lambda v_2) = \alpha\bar{\gamma} a(u_1, v_1) + \alpha\bar{\lambda} a(u_1, v_2) + \beta\bar{\gamma} a(u_2, v_1) + \beta\bar{\lambda} a(u_2, v_2).$$

A bilinear form $a : X \times X \to F$ is said to be symmetric if $a(u, v) = \overline{a(v, u)}, \forall u, v \in X$.

2.3 Review of Finite Element Method

In general, a closed form solution to a partial differential equation like the one in (2.9) is often unavailable, which makes it very difficult to solve it analytically. Numerical techniques are therefore employed to obtain a "truth" approximation – a numerical approximation that is sufficiently accurate such that the resulting approximate solution is indistinguishably close to the exact solution. The finite element method is among the most frequently used numerical techniques because of its various advantages, such as fast convergence and easy handling of geometries.

2.3.1 Variational or weak formulation

The point of departure for finite element method is a weighted-integral statement of the differential equation, called the *variational formulation*, or *weak formulation*. The weak form allows for more general solution spaces as well as natural boundary and continuity conditions of the problem.

We use a simple two-dimensional Laplacian eigenvalue problem as the example to review the finite element method,

$$-\nabla \cdot \mu \nabla u = \lambda u, \qquad \text{on } \Omega. \tag{2.11}$$

A periodic boundary condition is imposed on the boundary of Ω, denoted by Γ, to align with our physical problems later. To derive the weak form of the governing equation, we first introduce a function space

$$X^e = \{v \in H^1(\Omega)\}, \tag{2.12}$$

where

$$H^1(\Omega) = \{v \in L^2(\Omega) |\ \nabla v \in (L^2(\Omega))^d\}. \tag{2.13}$$

The associated norm is defined as

$$\|v\|_{X^e} = \left(\sum_{i=1}^{d} \|v_i\|^2_{H^1(\Omega)} \right)^{1/2}, \tag{2.14}$$

where d indicates the dimension of the computation domain. Multiplying (2.11) by a test function $v \in X^e$ and integrating by parts gives,

$$\int_\Omega \frac{\partial v}{\partial x} \mu \frac{\partial u}{\partial x} + \int_\Omega \frac{\partial v}{\partial y} \mu \frac{\partial u}{\partial y} = \lambda \int_\Omega uv. \tag{2.15}$$

Hence, the weak form of an eigenvalue problem can be stated as follows: find a solution pair $(\lambda_q, u_q^e(\mu)) \in \mathbb{R} \times X^e$ that satisfies

$$\begin{aligned} a(u_q^e(\mu), v; \mu) &= \lambda_q m(u_q^e(\mu), v), \quad \forall v \in X^e \\ m(u_q^e(\mu), u_\ell^e(\mu)) &= \delta_{q\ell}, \qquad q, \ell = 1, 2, \ldots, \end{aligned} \tag{2.16}$$

where

$$a(u, v; \mu) = \int_\Omega \frac{\partial v}{\partial x} \mu \frac{\partial u}{\partial x} + \int_\Omega \frac{\partial v}{\partial y} \mu \frac{\partial u}{\partial y}, \qquad m(u, v) = \int_\Omega uv.$$

Here $a(\cdot, \cdot; \mu)$ and $m(\cdot, \cdot)$ are μ-parameterized, and μ-independent bilinear forms respectively; $\delta_{q\ell}$ is the Kronecker delta which is defined as $\delta_{q\ell} = 1$ for $q = \ell$, and $\delta_{q\ell} = 0$ for $q \neq \ell$.

2.3.2 Spaces and basis

In the finite element method, one seeks an approximate solution over a discretized domain, known as a triangulation $\mathcal{T}_h$ of the physical domain $\Omega : \overline{\Omega} = \bigcup_{T_h \in \mathcal{T}_h} \overline{T}_h^k$, where $T_h^k, k = 1, \ldots, K$, are the elements, and $x_i, i = 1, \ldots, \mathcal{N}$, are the nodes. That is, $\overline{\Omega}$ is the sum of $\overline{T}_h^k$ (closure of elements). The subscript h denotes the diameter of the triangulation $\mathcal{T}_h$ and is the maximum of the longest edges of all the elements. Next, we define a finite element "truth" approximation space $X \in X^e$,

$$X = \{v \in X^e | v_{T_h} \in \mathcal{P}^p(T_h), \forall T_h \in \mathcal{T}_h\},$$

where $\mathcal{P}^p(T_h)$ is the space of p^{th} degree of polynomials over element T_h.

To obtain the discrete equations of the weak form, we approximate the field

variables $u_q(\mu)$ as as a linear combination of the basis functions $\varphi_i \in X, \varphi_i(x_j) = \delta_{ij}$ such that

$$u_q(\mu) = \sum_{i=1}^{\mathcal{N}} u_{qi}(\mu)\varphi_i, \tag{2.17}$$

where the "truth" space is now constructed as

$$X = \text{span}\{\varphi_1, \ldots, \varphi_{\mathcal{N}}\},$$

and $u_{qi}(\mu), i = 1, \ldots, \mathcal{N}$, is the nodal value of $u_q(\mu)$ at node x_i.

2.3.3 Discrete equations

Applying the Galerkin projection on the discrete "truth" space X, we can substitute (2.17) into (2.16), take the test function v as the basis function $\varphi_i, i = 1, \ldots, \mathcal{N}$, and obtain the linear system

$$\begin{aligned} &\sum_{j=1}^{\mathcal{N}} a(\varphi_j, \varphi_i; \mu) u_{qj} = \sum_{j=1}^{\mathcal{N}} \lambda_h m(\varphi_j, \varphi_i) u_{qj}, \quad i = 1, \ldots, \mathcal{N}, \\ &\sum_{i=1}^{\mathcal{N}} \sum_{j=1}^{\mathcal{N}} m(\varphi_j, \varphi_i) u_{qi} u_{\ell j} = \delta_{q\ell}, \quad q, \ell = 1, \ldots, \mathcal{N}, \end{aligned} \tag{2.18}$$

which can be rewritten into matrix form

$$A_h(\mu) u_{qh}(\mu) = \lambda_{qh} M_h u_{qh}(\mu). \tag{2.19}$$

Here A_h is an $\mathcal{N} \times \mathcal{N}$ symmetric stiffness matrix with $A_{ij}(\mu) = a(\varphi_j, \varphi_i; \mu)$, M_h is of the same size $\mathcal{N} \times \mathcal{N}$ positive definite mass matrix with $M_{ij} = m(\varphi_j, \varphi_i)$, and $u_{qh}(\mu)$ is a vector with $u_{qi}(\mu) = u_q(x_i; \mu)$. Besides the explicit partial differential equation, the stiffness matrix and mass matrix also depend closely on the finite element discretization, e.g., the triangulation, the basis functions for the solution approximation, and the shape functions for the geometry interpolation. They are normally formed via elemental (T_h of $\mathcal{T}_h$) matrices assembly. For a more detailed discussion and implementation of the finite element procedure, one can refer to various finite element method textbooks (e.g.,[6]).

2.4 Review of Convex Optimization

A convex optimization problem is one of the form,

$$\begin{aligned} &\text{minimize} && f_0(x) \\ &\text{subject to} && f_i(x) \leq b_i, \quad i = 1, \ldots, n, \end{aligned} \tag{2.20}$$

where $f_0, f_1, \ldots, f_n : \mathbb{R}^m \to \mathbb{R}$ are convex functions, i.e.,

$$f_i(\alpha x + (1-\alpha)y) \leq \alpha f_i(x) + (1-\alpha) f_i(x),$$

for all $x, y \in \mathbf{R}^m$, and for all $\alpha \in [0, 1]$. Equality constraints can be treated equivalently by a pair of inequality constraints ($h(x) = 0 \Leftrightarrow h(x) \leq 0$ and $h(x) \geq 0$), therefore they can be removed from our standard form for theoretical purpose. Both the least-squares problem and the linear programming problem are widely known subclasses of the general convex optimization problems. In the following sections, we will focus on reviewing two relatively recent classes that are extensively employed throughout this work: semidefinite program and second-order cone program. However, some important concepts have to be briefly defined first, e.g., convex sets and cones, as well as generalized inequalities. More details on convex optimization and related topics are covered in [2, 13].

Following the standard notations in literature, we use $\mathbb{R}$ to denote the set of real numbers, $\mathbb{R}_+$ to denote the set of nonnegative real numbers, and $\mathbb{R}_{++}$ to denote the positive real numbers. To denote the set of real n-vectors, and the set of $m \times n$ matrices, $\mathbb{R}^n$ and $\mathbb{R}^{m \times n}$ are used respectively.

2.4.1 Convex sets and cones

Convex sets

A set $\mathbf{C}$ is a *convex* set if the line segment between any two points in $\mathbf{C}$ lies in $\mathbf{C}$, i.e., $\forall x, y \in \mathbf{C}$, and $\forall \alpha \in [0, 1]$,

$$\alpha x + (1-\alpha)y \in \mathbf{C}.$$

A loose way to visualize a convex set is one in which every point in the set can be seen by every other point, along an unobstructed straight path between them, where "unobstructed" means being confined inside the set.

Cones

A set $\mathbf{C}$ is a *cone* (or *nonnegative homogeneous*), if for every $x \in \mathbf{C}$ and $\alpha \geq 0$, there is $\alpha x \in \mathbf{C}$. A *convex cone* is a set $\mathbf{C}$ that is both convex and is a cone. In other words, a set $\mathbf{C}$ is a convex cone if $\forall x, y \in \mathbf{C}$, and any $\alpha, \beta \geq 0$, we have,

$$\alpha x + \beta y \in \mathbf{C}.$$

Proper cones

A *proper cone* is a cone $\mathcal{K} \subseteq \mathbb{R}^n$ that satisfies the following:

1. $\mathcal{K}$ is convex;
2. $\mathcal{K}$ is closed;
3. $\mathcal{K}$ is *solid*, i.e., it has nonempty interior;
4. $\mathcal{K}$ is *point*, i.e., it contains no line; or equivalently, $x \in \mathcal{K}, -x \in \mathcal{K} \rightarrow x = 0$.

Generalized inequalities

A *generalized inequality* can be defined over a proper cone $\mathcal{K}$. The notation of generalized inequalities is meant to suggest the analogy to ordinary inequality on $\mathbb{R}$. Hence, it has many of the similar properties. A generalized inequality is a partial ordering on $\mathbb{R}^n$ as an extension of the standard ordering on $\mathbb{R}$. It is associated with the proper one $\mathcal{K}$ and defined by

$$x \preceq_{\mathcal{K}} y \Leftrightarrow y - x \in \mathcal{K}.$$

Similarly, an associated strict partial ordering is defined by

$$x \prec_{\mathcal{K}} y \Leftrightarrow y - x \in \text{int}\mathcal{K}.$$

where int$\mathcal{K}$ indicates the interior of $\mathcal{K}$. When $\mathcal{K} = \mathbb{R}_+$, the partial ordering $\preceq_{\mathcal{K}}$ becomes the standard ordering on $\mathbb{R}$, and the strict partial ordering $\prec_{\mathcal{K}}$ is equivalent to the strict inequality $<$ on $\mathbb{R}$.

Positive semidefinite cone

We use $\mathbf{S}^k$ to denote the set of symmetric $k \times k$ matrices,

$$\mathbf{S}^k := \{X \in \mathbb{R}^{k \times k} | X = X^T\}.$$

Note that $\mathbf{S}^k$ is a vector space with dimension $k(k+1)/2$. Analogously, $\mathbf{S}^k_+$ is used to denote the set of symmetric positive semidefinite matrices:

$$\mathbf{S}^k_+ := \{X \in \mathbf{S}^k | X \succeq 0\},$$

and $\mathbf{S}^k_{++}$ to denote the set of symmetric positive definite matrices:

$$\mathbf{S}^k_{++} := \{X \in \mathbf{S}^k | X \succ 0\}.$$

Since the partial ordering on $\mathbf{S}_+$ and $\mathbf{S}_{++}$ arises frequently throughout this thesis, the subscript is dropped whenever there is no chance of confusion: $X \succeq 0$ and $X \succ 0$ imply positive semidefiniteness and positive definiteness for symmetric matrix X.

Second-order cone

A second-order cone of dimension $q+1$ is defined as,

$$\mathcal{Q}^{q+1} = \{\boldsymbol{x} = (x_0; \bar{\boldsymbol{x}}) \in \mathbb{R}^{q+1} |\ x_0 \geq \|\bar{\boldsymbol{x}}\|\},$$

where $\|\cdot\|$ refers to the standard Euclidean norm. The second-order cone inequality is denoted by $\boldsymbol{x} \succeq_{\mathcal{Q}} 0$. Notice that in this expression, the dimension of the cone is dropped for succinctness.

2.4.2 Semidefinite program

The conic form of a semidefinite program (SDP) is defined as,

$$\begin{array}{ll} \text{minimize} & c^T x \\ \text{subject to} & F_0^i + x_1 F_1^i + \cdots x_m F_m^i \preceq_{\mathbf{S}^{k_i}} 0, \quad i = 1, \ldots, n, \\ & Ax = b, \end{array} \tag{2.21}$$

where $F_0^i, F_1^i, \cdots F_m^i \in \mathbf{S}^{k^i}, i = 1, \ldots, n$, i.e., symmetric matrices of dimension $k_i \times k_i$, and $A \in \mathbb{R}^{p \times m}$. The generalized inequality in (2.21) is called a linear matrix inequality (LMI). (2.21) reduces to a linear program when $F_0^i, F_1^i, \cdots F_m^i, i = 1, \ldots, n$ are diagonal.

2.4.3 Second-order cone program

Similarly, the second-order cone program (SOCP) can be expressed as a conic form problem:

$$\begin{array}{ll} \text{minimize} & c^T x \\ \text{subject to} & Q_i x \preceq_{\mathcal{K}_i} 0, \quad i = 1, \ldots, n, \\ & Ax = b, \end{array} \tag{2.22}$$

where

$$\mathcal{K}_i = \{[x_0; \bar{\boldsymbol{x}}] \in \mathbb{R}^{q_i+1} |\ x_0 \geq \|\bar{\boldsymbol{x}}\|\},$$

is a second-order cone in $\mathbb{R}^{q_i+1}$. The matrices $Q_i \in \mathbb{R}^{(q_i+1)\times m}$ and $A \in \mathbb{R}^{p \times m}$.

2.4.4 Linear fractional program

Another special class of problems worth mentioning which will appear in our formulations in later chapters: is called *linear-fractional program*. The problem is to minimize a ratio of affine functions over a polyhedron:

$$\begin{array}{ll} \text{minimize} & \frac{a^T \boldsymbol{x} + b}{c^T \boldsymbol{x} + d} \\ \text{subject to} & F\boldsymbol{x} \preceq g, \\ & A\boldsymbol{x} = f. \end{array} \tag{2.23}$$

By change of variables,

$$\boldsymbol{y} = \frac{\boldsymbol{x}}{c^T\boldsymbol{x} + d}, \qquad z = \frac{1}{c^T\boldsymbol{x} + d}, \tag{2.24}$$

program (2.23) can be transformed to a linear program:

$$\begin{aligned} \text{minimize} \quad & a^T\boldsymbol{y} + bz \\ \text{subject to} \quad & F\boldsymbol{y} - gz \preceq 0, \\ & A\boldsymbol{y} - fz = 0, \\ & c^T\boldsymbol{y} + dz = 1, \\ & z \geq 0. \end{aligned} \tag{2.25}$$

(2.23) is in the form that can be handled by most standard optimization solvers.

Chapter 3

Band Structure Calculation

In this chapter, we will focus on the numerical calculations of the Maxwell equations in the form of Hermitian eigenvalue problems. Two physical problems will be introduced, the two-dimensional photonic crystal and the three-dimensional photonic crystal fiber. Next, the eigenvalue problem based governing equations and finite element method based solution methods will be derived and solved. Mesh adaptivity will also be introduced for more efficient representation of the material properties. These numerical recipes are the essential premise to the optimal design problems in Chapters 4 and 5.

The propagation of electromagnetic waves in photonic crystals is governed by Maxwell's equations, which have been cast as linear Hermitian eigenvalue problems (3.1), assuming the electromagnetic waves are monochromatic in (2.4) and (2.5):

$$\boldsymbol{\nabla} \times \left(\varepsilon(\boldsymbol{r})^{-1} \boldsymbol{\nabla} \times \boldsymbol{H}(\boldsymbol{r})\right) = \left(\frac{\omega}{c}\right)^2 \boldsymbol{H}(\boldsymbol{r}), \qquad \text{in } \mathbb{R}^3, \tag{3.1a}$$

$$\varepsilon(\boldsymbol{r})^{-1} \boldsymbol{\nabla} \times (\boldsymbol{\nabla} \times \boldsymbol{E}(\boldsymbol{r})) = \left(\frac{\omega}{c}\right)^2 \boldsymbol{E}(\boldsymbol{r}), \qquad \text{in } \mathbb{R}^3. \tag{3.1b}$$

In addition, we need to add the two divergence free conditions to ensure no point source or sinks of magnetic fields and displacement in the medium:

$$\boldsymbol{\nabla} \cdot \boldsymbol{H}(\boldsymbol{r}) = 0, \qquad \boldsymbol{\nabla} \cdot \left(\varepsilon(\boldsymbol{r})^{-1} \boldsymbol{E}(\boldsymbol{r})\right) = 0, \qquad \text{in } \mathbb{R}^3. \tag{3.1c}$$

The solutions to these equations are in general very complex functions of space

and time; numerical computations are hence crucial for any further analysis. Established frequency-domain numerical methods include finite difference method, spectral method and boundary element method. Please refer to appendix D of [29] for a more comprehensive survey of the available computational methods. Finite element method is chosen in our work for eigenvalue computation (this chapter) and the optimization problems (chapters 4 and 5), mainly for the following reasons:

Geometry representation. Finite element method is known for representing complicated geometries with high accuracy using suitable unstructured computational meshes. One might argue that this is not an obvious advantage of the method when used in topology optimization, since structured meshes are normally used. However, the superiority of the method lies in its ability to handle complicated geometries with structured, but non-uniform meshes with ease. It will be made clearer in the next bullet point;

Mesh Adaptivity. While structured meshes are called for in the topology optimization, one can use successively refined non-uniform, yet still structured adaptive meshes to achieve more accurate representation of the geometries during the optimization process. Finite element method undoubtedly excels in accomplishing this task.

Parameter sensitivity and affinity. As we shall soon see, the governing equations in our problems are either linear in the design variables (material property: dielectric function ε) or linear with respect to its reciprocal. Thanks to the use of the finite element methods (in fact, many other numerical methods would also maintain the linearity in the discrete systems), after reformulating the optimization problem into convex programs in chapters 4 and 5, we can easily transfer the eigenvalue sensitivity with respect to the design variables, to the relevant matrices sensitivity with respect to the design variables. While the eigenvalue sensitivity has a nonlinear relation and is non-differentiable at eigenvalue degeneracy, the matrices sensitivity can be easily rewritten in a linear fashion with some

changes of variables.

3.1 Band Structure of Two-dimensional Photonic Crystal Structure

3.1.1 Governing equations

In a two-dimensional photonic crystal, periodicity occurs across two of its axes (e.g., $xy-$plane), and the structure is homogeneous along the third axis (e.g., z-axis). There are two possible polarizations of the electromagnetic waves propagating in such a structure: transverse electric (TE) polarization, and transverse magnetic (TM) polarization. For TE polarization, the electric field $\boldsymbol{E}^{TE}(\boldsymbol{r}) = (E_x, E_y, 0)$ is confined to the plane of wave propagation, while the magnetic field $\boldsymbol{H}^{TE}(\boldsymbol{r}) = (0, 0, H)$ is perpendicular to this plane. Conversely, for TM polarization, the magnetic field $\boldsymbol{H}^{TM}(\boldsymbol{r}) = (H_x, H_y, 0)$ is confined to the plane of wave propagation, while the electric field $\boldsymbol{E}^{TM}(\boldsymbol{r}) = (0, 0, E)$ is perpendicular to this plane. In such cases, the Maxwell equations can be reduced to scalar eigenvalue problems:

$$\text{TE}: \qquad -\boldsymbol{\nabla}\cdot\left(\varepsilon^{-1}(\boldsymbol{r})\boldsymbol{\nabla}H(\boldsymbol{r})\right) = \left(\frac{\omega}{c}\right)^2 H(\boldsymbol{r}), \qquad \text{in } \mathbb{R}^2, \tag{3.1.1a}$$

$$\text{TM}: \qquad -\boldsymbol{\nabla}\cdot\left(\boldsymbol{\nabla}E(\boldsymbol{r})\right) = \left(\frac{\omega}{c}\right)^2 \varepsilon(\boldsymbol{r})E(\boldsymbol{r}), \qquad \text{in } \mathbb{R}^2\ . \tag{3.1.1b}$$

Note that the reciprocal of the dielectric function is present in the differential operator for the TE case, whereas the dielectric function is present in the right-hand side for the TM case.

We consider two of the most common types of a two-dimensional lattice for the arrangement of dielectric materials: the square lattice and the hexagonal lattice, depicted in Figure 3.1. Recall that the dielectric material of a photonic crystal satisfies a periodic function of the form $\varepsilon(\boldsymbol{r}) = \varepsilon(\boldsymbol{r}+\boldsymbol{R})$ for all vectors $\boldsymbol{R}$, where $\boldsymbol{R}$ are the lattice vectors spanned by the primitive lattice vectors $\{\boldsymbol{a}_1, \boldsymbol{a}_2\}$ which translate the lattice into itself. There are many ways of representing the primitive lattice vectors $\boldsymbol{a}_1$ and $\boldsymbol{a}_2$ for different lattices, one of which is shown in Figure 3.1. In this representation, the square lattice has $\boldsymbol{a}_1 = a\hat{\boldsymbol{x}}$, and $\boldsymbol{a}_2 = a\hat{\boldsymbol{y}}$;

and the hexagonal lattice has $\boldsymbol{a}_1 = a\hat{\boldsymbol{x}}$, and $\boldsymbol{a}_2 = a(\hat{\boldsymbol{x}} + \hat{\boldsymbol{y}}\sqrt{3})/2$.

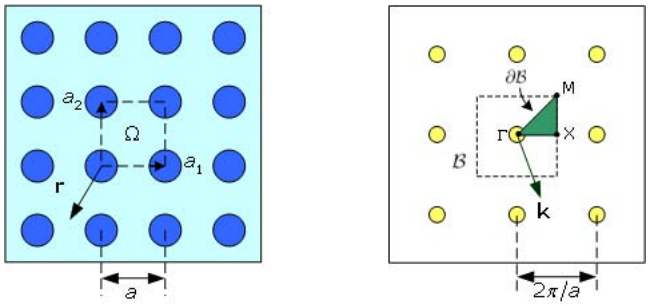

(a) Square lattice

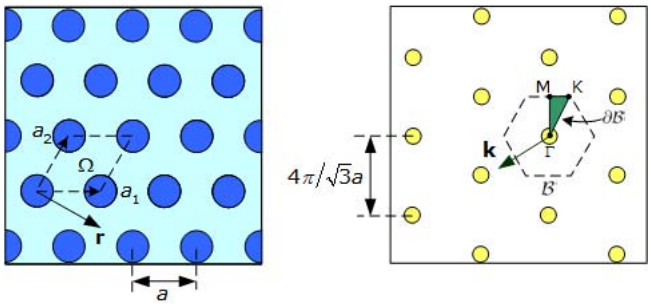

(b) Rhombic lattice

Figure 3.1: Left: A photonic crystal on a square lattice (top), and on a hexagonal lattice (bottom). The dashed box represents the primitive unit cell (Ω), where a is the periodicity length of the lattice. Right: The respective reciprocal lattices. The dashed box represents in each case the first Brillouin zone ($\mathcal{B}$). The irreducible zone is shown as the green triangular wedge, with its boundary denoted by $\partial\mathcal{B}$.

Bloch-Floquet theory introduced in section 2.1.2 states that the solution to the periodic eigenvalue problems (3.1.1) is of the form

$$H(\boldsymbol{r}) = H_{\boldsymbol{k}}(\boldsymbol{r})e^{i\boldsymbol{k}\cdot\boldsymbol{r}}, \quad \text{and} \quad E(\boldsymbol{r}) = E_{\boldsymbol{k}}(\boldsymbol{r})e^{i\boldsymbol{k}\cdot\boldsymbol{r}},$$

where $H_{\boldsymbol{k}}(\boldsymbol{r})$ and $E_{\boldsymbol{k}}(\boldsymbol{r})$ are periodic envelope functions. Substituting these into (3.1.1), we can show that $H_{\boldsymbol{k}}(\boldsymbol{r})$ and $E_{\boldsymbol{k}}(\boldsymbol{r})$ are now the eigenfunctions of slightly different Hermitian eigenvalue problems respectively,

$$\text{TE}: \qquad (\boldsymbol{\nabla} + i\boldsymbol{k}) \cdot \left(\frac{1}{\varepsilon(\boldsymbol{r})}(\boldsymbol{\nabla} + i\boldsymbol{k})H_{\boldsymbol{k}}(\boldsymbol{r})\right) = \left(\frac{\omega}{c}\right)^2 H_{\boldsymbol{k}}(\boldsymbol{r}), \qquad \text{in } \Omega, \quad (3.1.2a)$$

$$\text{TM}: \qquad (\boldsymbol{\nabla} + i\boldsymbol{k}) \cdot ((\boldsymbol{\nabla} + i\boldsymbol{k})E_{\boldsymbol{k}}(\boldsymbol{r})) = \left(\frac{\omega}{c}\right)^2 \varepsilon(\boldsymbol{r})E_{\boldsymbol{k}}(\boldsymbol{r}), \qquad \text{in } \Omega. \quad (3.1.2b)$$

Thus, the effect of considering periodicity amounts to replacing the indefinite periodic domain by the unit cell Ω and $\boldsymbol{\nabla}$ by $\boldsymbol{\nabla} + i\boldsymbol{k}$ in the original equations.

$\boldsymbol{k}$ is a wave vector in the first Brillouin zone $\mathcal{B}$.

For notational convenience, we write the above equations in the following operator form:

$$\mathcal{A}u = \lambda \mathcal{M}u, \qquad \text{in } \Omega. \tag{3.1.3}$$

For the TE case, $u \equiv H_{\boldsymbol{k}}(\boldsymbol{r})(\in H^1(\Omega) \equiv \left\{v \in L^2(\Omega) \mid \nabla_\perp v \in (L^2(\Omega))^2\right\})$, $\lambda \equiv \omega_{\mathrm{TE}}^2/c^2$, and

$$\mathcal{A}(\varepsilon, \boldsymbol{k}) \equiv -(\boldsymbol{\nabla} + i\boldsymbol{k}) \cdot \left(\frac{1}{\varepsilon(\boldsymbol{r})}(\boldsymbol{\nabla} + i\boldsymbol{k})\right). \qquad \mathcal{M} \equiv I; \tag{3.1.4a}$$

For the TM case, $u \equiv E_{\boldsymbol{k}}(\boldsymbol{r})(\in H^1(\Omega))$, $\lambda \equiv \omega_{\mathrm{TM}}^2/c^2$, and

$$\mathcal{A}(\boldsymbol{k}) \equiv -(\boldsymbol{\nabla} + i\boldsymbol{k}) \cdot (\boldsymbol{\nabla} + i\boldsymbol{k}), \qquad \mathcal{M}(\varepsilon) \equiv \varepsilon(\boldsymbol{r})I, \tag{3.1.4b}$$

In the equations (3.1.4), I denotes the identity operator. We denote by (u^m, λ^m) the m-th pair of eigenfunction and eigenvalue of (3.1.3) and assume that these eigen pairs are numbered in ascending order: $0 < \lambda^1 \leq \lambda^2 \leq \cdots \leq \lambda^\infty$.

3.1.2 Discretization

Next, we need to discretize the above infinite dimensional eigenvalue problem so that it can be handled numerically.

This process involves three steps. First, we discretize the boundary of the irreducible Brillouin zone $\partial\mathcal{B}$, so that only n_k wave vectors are considered (Figure 3.2). The choice of solving the eigenproblem only on the irreducible Brillouin boundary is driven by the band gap calculation and the optimization problem, as the optima of the eigenvalues of the underlying eigenproblem are shown to usually occur on $\partial\mathcal{B}$. Therefore,

$$\mathcal{P}_h := \{\boldsymbol{k}_t \in \partial\mathcal{B}, 1 \leq t \leq n_k\}. \tag{3.1.5}$$

Second, the unit cell Ω is decomposed into N disjoint subcells $K_i, 1 \leq i \leq N$, such that $\Omega = \cup_{i=1}^N K_i$, and the shared interface of two neighboring elements K_i and K_j is denoted by e_{ij}. This subcell grid is then used to represent the dis-

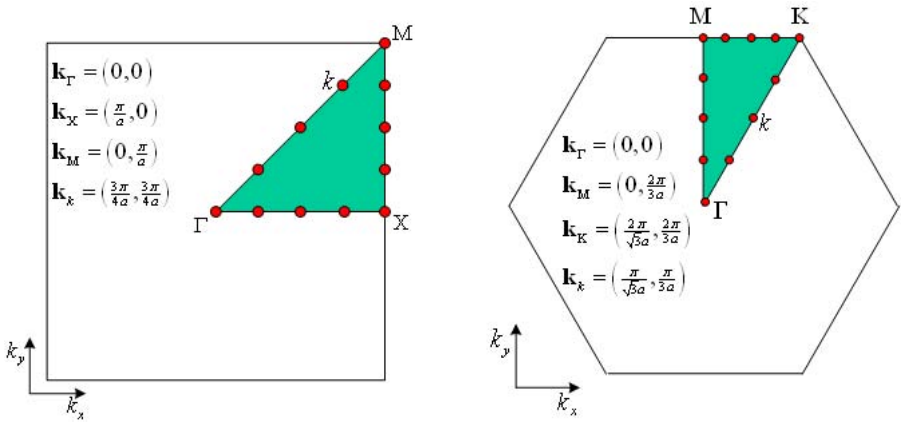

(a) Square lattice (b) Hexagonal lattice

Figure 3.2: The shaded wedges denote in each case the irreducible brillouin zone of (a) square lattice and (b) hexgonal lattice. The red dots are the representative discrete wave vectors.

tribution of dielectric function discretely, as shown in Figure 3.3. Our dielectric function $\varepsilon(\boldsymbol{r})$ takes a uniform value between ε_L and ε_H on each cell, where ε_L and ε_H are dielectric constants of a low-index material and a high-index material respectively that make up the composite of the photonic crystal. That is $\varepsilon(\boldsymbol{r}) = \varepsilon_j (\in \mathbb{R})$ on K_i, and $\varepsilon_L \leq \varepsilon_j \leq \varepsilon_H$. Moreover, if the symmetry of the prescribed lattice is taken into consideration, the dielectric function only needs to be defined in 1/8 of the unit cell in a square lattice, or in 1/12 of the unit cell in a hexagonal lattice, namely,

$$\mathcal{Q}_h = \{\boldsymbol{\varepsilon} : \boldsymbol{\varepsilon} \in [\varepsilon_L, \varepsilon_H]^{n_\varepsilon}\}, \tag{3.1.6}$$

where $n_\varepsilon < N^2 \equiv \mathcal{N}$.

Third, a discrete subcell triangulation $\mathcal{T}_h$ is used to approximate the finite element solution of the system (3.1.3). A finite element "truth" approximation space X_h of complex valued functions is defined as

$$X_h = \left\{v \in H^1(\Omega) \mid v|_K \in \mathcal{P}^p(K), \forall K \in \mathcal{T}_h\right\}, \tag{3.1.7}$$

where $\mathcal{P}^p$ is the space of complex valued polynomials of total degree at most $p = p_{RE} + p_{IM}$ on K. It is known that either increasing the interpolation polynomial degree p or decreasing the mesh size h or both lead to a more accurate

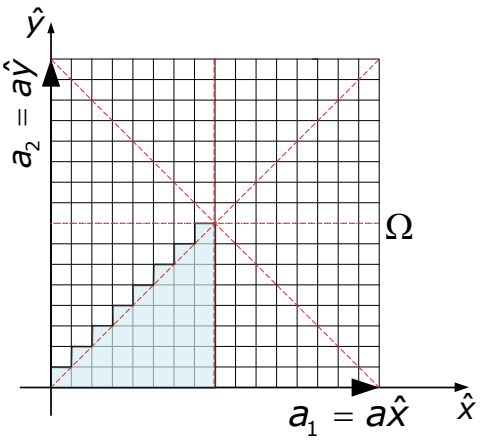

(a) Square lattice

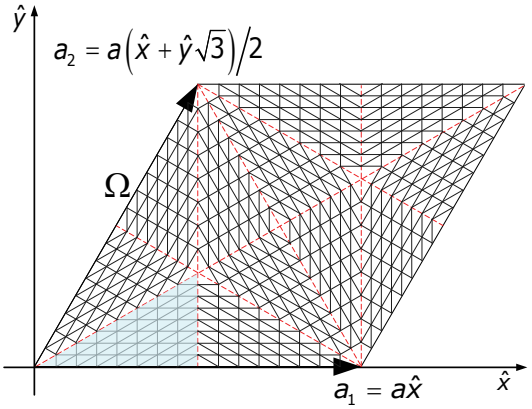

(b) Hexagonal lattice

Figure 3.3: Dielectric variables are defined on the highlighted cells; the rest are obtained through symmetry. The red dashes indicate the symmetry lines.

approximation of the solution. While both $p-$ and $h-$ refinement schemes result in more degrees of freedom for the system, hence increased computation cost, $p-$refinement approach almost always provides an advantageous convergence. However, in topology optimization [9], where the material properties of each subcell are the optimization decision variables, the capacity of efficient geometry representation is prior to higher convergence. This is why in all our computation and optimization simulations followed, low order interpolation polynomials (mostly, $p = 1$ is used) are employed on fine computational meshes. As part of the finite element discretization of step three, the equations in (3.1.3) are multiplied by a test function $v \in X_h$, and integrated by parts to obtain the weak

forms:

$$\int_\Omega \frac{1}{\varepsilon}\nabla v\cdot\nabla H_{\boldsymbol{k}}d\Omega + i\boldsymbol{k}\cdot\int_\Omega \frac{1}{\varepsilon}(H_{\boldsymbol{k}}\nabla v - v\nabla H_{\boldsymbol{k}})d\Omega + \boldsymbol{k}\cdot\boldsymbol{k}\int_\Omega \frac{1}{\varepsilon}vH_{\boldsymbol{k}}d\Omega = \lambda\int_\Omega vH_{\boldsymbol{k}}d\Omega, \tag{3.1.8a}$$

$$\int_\Omega \nabla v\cdot\nabla E_{\boldsymbol{k}}d\Omega + i\boldsymbol{k}\cdot\int_\Omega (E_{\boldsymbol{k}}\nabla v - v\nabla E_{\boldsymbol{k}})d\Omega + \boldsymbol{k}\cdot\boldsymbol{k}\int_\Omega vE_{\boldsymbol{k}}d\Omega = \lambda\int_\Omega \varepsilon vE_{\boldsymbol{k}}d\Omega. \tag{3.1.8b}$$

We obtain the discrete equations of the weak forms,

$$A_h(\boldsymbol{\varepsilon},\boldsymbol{k})u_h^{m_j} = \lambda_h^{m_j}M_h(\boldsymbol{\varepsilon})u_h^{m_j}, \quad \boldsymbol{\varepsilon}\in\mathcal{Q}_h, \boldsymbol{k}\in\mathcal{P}_h, \tag{3.1.9}$$

where $A_h(\boldsymbol{\varepsilon},\boldsymbol{k})\in\mathbb{C}^{\mathcal{N}\times\mathcal{N}}$ is a Hermitian matrix and $M_h(\boldsymbol{\varepsilon})\in\mathbb{R}^{\mathcal{N}\times\mathcal{N}}$ is a symmetric positive definite matrix. Since $\varepsilon(\boldsymbol{r})$ is piecewise-constant on Ω, the $\varepsilon-$dependent matrices can be expressed as

$$A_h^{TE}(\boldsymbol{\varepsilon},\boldsymbol{k}) = \sum_{i=1}^{n_\varepsilon}\varepsilon_i^{-1}A_{h,i}^{TE}(\boldsymbol{k}), \quad M_h^{TM}(\boldsymbol{\varepsilon}) = \sum_{i=1}^{n_\varepsilon}\varepsilon_i M_{h,i}^{TM}, \tag{3.1.10a}$$

while $A_h^{\mathrm{TM}}(\boldsymbol{k})$ and M_h^{TE} are independent of ε, and can be expressed as

$$A_h^{TM}(\boldsymbol{k}) = \sum_{i=1}^{n_\varepsilon}A_{h,i}^{TM}(\boldsymbol{k}), \quad M_h^{TE} = \sum_{i=1}^{n_\varepsilon}M_{h,i}^{TE},. \tag{3.1.10b}$$

In the equations (3.1.10) and following, superscripts $^{\mathrm{TM}}$ and $^{\mathrm{TE}}$ are used to indicate TM polarization and TE polarization, respectively. The subscripts $_i$ of the matrices contain the contribution of all the elements indexed by dielectric variable ε_i.

Equations (3.1.10a) and (3.1.10b) can then be solved by standard eigen solvers. "eigs" from MATLAB® is chosen in our implementation as it also exploits the sparsity of the matrices.

3.1.3 Mesh refinement

Uniform structured mesh has been used for the previous discretizations of dielectric function and eigenvalue problem (section 3.1.2). To improve the efficiency of the discretization while preserving the accuracy, we explore adaptive mesh

refinement in this section. The primary objective of adaptive mesh refinement is to capture the details of material property more efficiently and to resolve the field solutions accurately. One strategy to increase the discretization resolution is to allocate more degrees of freedom, hence more computational nodes, in regions where the eigenfunctions have higher gradient, and to maintain a coarser discretization in regions of smooth solutions. In our problem where the computation domain consists of materials of two different dielectric constants, increased variation in the eigenfunctions can typically be expected along the material interfaces. Given any initial coarse representation of the optimal crystal configuration, we will only further subdivide those elements meeting the refinement criteria, and allow more degrees of freedom in both the field variables (by increasing $\mathcal{N}$ in (3.1.9)) and optimization decision variables (by increasing n_ε in (3.1.6)). Practically, a quadrilateral element is simply subdivided into 4 smaller elements by connecting the mid points of its edges, as shown in Figure 3.4.

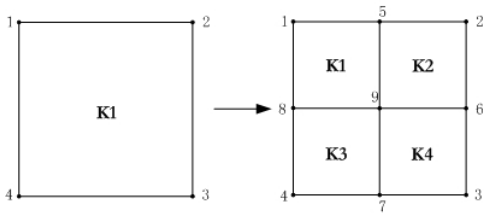

(a) Quadrilateral element

Figure 3.4: Mesh elements can be refined by connecting mid-points of the edges and creating three more elements.

Care should be given to the choice of the refinement criteria to ensure both the efficiency and accuracy of the computation. The efficiency of the adaptive refinement is accomplished by correctly identifying the elements on the material interface that should be subdivided. An element is categorized as an *interface element* if any of its neighbors has different material property (ε) than his own. By the same token, this different neighbor will also be classified as an interface element. This principle is illustrated in Figure 3.5 using quadrilateral elements. In our implementation, the element connectivity of the mesh structure is used to locate all the $4 - 8$ neighbors of any element. The cost of this search is only of order $\mathcal{O}(\log \mathcal{N}_t^{(r)})$, where $\mathcal{N}_t^{(r)}$ is the number of elements at the current refinement level r.

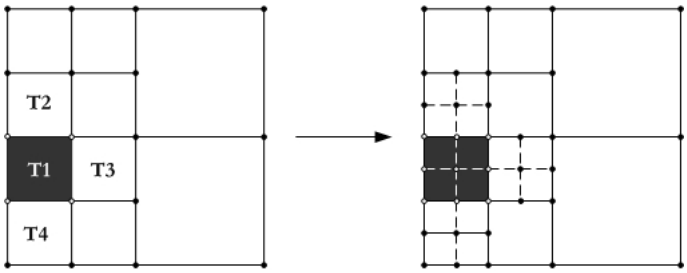

Figure 3.5: In this illustration, elements T_2, T_3, T_4 all are of different material property from their adjacent element T_1, and conversely, element T_1 is of different material property than its neighbors T_2, T_3, T_4. According to our definition, they all fall under the category of *interface elements*. To refine these elements, their edges are bisected and connected to form finer regional mesh.

In such a way, hanging nodes are generated after each refinement if the adjacent elements are not of the same size. To ensure the conformability of the mesh and the consistency of the solution, the $2:1$ rule is applied to restrict the refinement level difference between adjacent elements. In our approach, an element, although not necessarily an *interface element*, will still be refined if one of its neighbors has been refined twice more than itself, demonstrated in Figure 3.6. By imposing such a restriction, we can ensure there is at most one hanging node along the edge of a relatively coarser element.

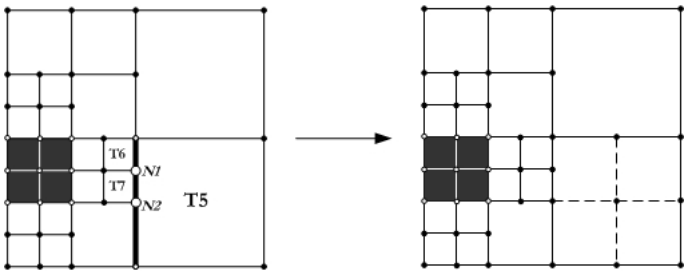

Figure 3.6: As a result of refining element T_3 in Figure 3.5, two hanging nodes N_1 and N_2 are created along the left edge of element T_5. This leads to the violation of the $2:1$ rule, as both elements T_6 and T_7 have been refined twice more than T_5. Therefore, although T_5 is not on the material interface, it should be flagged and refined to ensure the conformability of the method.

Many methods have been proposed to handle the presence of hanging nodes, see [55] for a review of such methods. In this work where the structured mesh is used, the simplest strategy is to fix the value of the hanging node by a suitable (linear) interpolation using the corresponding neighboring regular nodes. In Figure 3.7, the field value at node $\vec{x}_5$, $U(\vec{x}_5)$ or simply U_5, is treated as a "spurious" degree of freedom, and its value is interpolated as $U(\vec{x}_5) = \frac{1}{2}(U(\vec{x}_4) + U(\vec{x}_6))$.

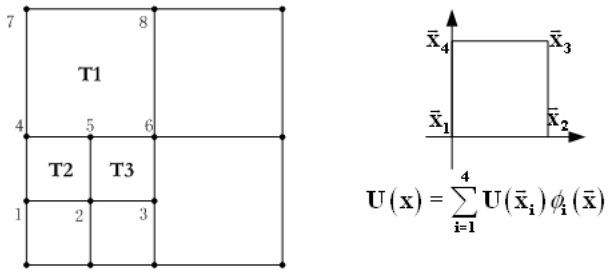

Figure 3.7: A quadtree mesh demonstrating several hanging nodes. Specifically, node 5 will be interpolated by the values of nodes 4 and 6. This is equivalent to using the modified basis functions – $\phi_3'(\vec{x}), \phi_4'(\vec{x})$ – for interpolating the field variable. A linear reference element is shown on the right.

Effectively, the field variable in T_2 can be represented as

$$\begin{aligned} U(\vec{x})_{T_2} &= U(\vec{x}_1)\phi_1(\vec{x}) + U(\vec{x}_2)\phi_2(\vec{x}) + U(\vec{x}_5)\phi_3(\vec{x}) + U(\vec{x}_4)\phi_4(\vec{x}) \\ &= U(\vec{x}_1)\phi_1(\vec{x}) + U(\vec{x}_2)phi_2(\vec{x}) + \frac{1}{2}(U(\vec{x}_4) + U(\vec{x}_6))\phi_3(\vec{x}) + U(\vec{x}_4)\phi_4(\vec{x}) \\ &= U(\vec{x}_1)\phi_1(\vec{x}) + U(\vec{x}_2)\phi_2(\vec{x}) + U(\vec{x}_6)\big(\tfrac{1}{2}\phi_3(\vec{x})\big) + U(\vec{x}_4)\big(\tfrac{1}{2}\phi_3(\vec{x}) + \phi_4(\vec{x})\big) \\ &= U(\vec{x}_1)\phi_1(\vec{x}) + U(\vec{x}_2)\phi_2(\vec{x}) + U(\vec{x}_6)\phi_3'(\vec{x}) + U(\vec{x}_4)\phi_4'(\vec{x}). \end{aligned} \tag{3.1.11}$$

The *refinement criteria* are summarized below:

- if two adjacent elements are of different material property (ε), both of them should be refined;
- if two adjacent elements have a refinement level difference more or equal than 2, the coarser one should be refined.

3.1.4 Results and discussion

Eigenvalue convergence on homogeneous domain

We start with the simplest problem where the material is homogeneous with dielectric constant $\varepsilon(\boldsymbol{r}) = 1$ everywhere. The analytical eigenvalue in this case is known to be $\lambda_j = (m\pi + k_x)^2 + (n\pi + k_y)^2,\ m, n \in \mathbb{Z}$ when the computation domain is $\Omega = [-1, 1]^2$. We consider quadrilateral meshes of both uniform and non-uniform size. The uniform mesh is obtained by splitting a regular $n \times n$ Cartesian grid into a total of n^2 squares, giving an uniform element size of

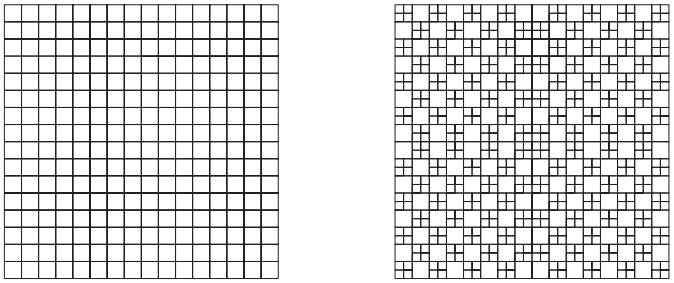

(a) Uniform mesh, $h = a/16$;

(b) Non-uniform mesh, $h_{equiv} = a/20.39$.

Figure 3.8: Homogeneous domain discretized by uniform mesh and nonuniform structured grids.

$h = a/n$. The non-uniform mesh is obtained by refining half of the elements of the uniform mesh, giving the smallest element size of $h_{\min} = a/(2n)$. Four different meshes are used in each case, $n = 8, 16, 32, 64$, and the eigenfunctions are obtained via interpolation polynomials of degree $p = 1$. Figure 3.8 illustrates the computation meshes used when $n = 16$. For the nonuniform meshes used in all the subsequent experiments, we define another more meaningful quantity, the equivalent mesh size:

$$h_{equiv} = a/\sqrt{N_{DOF}}.$$

Here, N_{DOF} represents the number of degrees of freedom of the system. In Figure 3.8(b) this number is also the remaining number of nodes after subtracting the number of hanging nodes.

The errors of the jth eigenvalue λ_h^j on a uniform mesh and $\lambda_{h_{equiv}}^j$ on a nonuniform mesh are defined as:

$$e_h^j = \|\lambda_h^j - \lambda^j\|/\|\lambda^j\|, \tag{3.1.12a}$$

$$e_{h_{equiv}}^j = \|\lambda_{h_{equiv}}^j - \lambda^j\|/\|\lambda^j\|. \tag{3.1.12b}$$

In Figure 3.9, the errors of the computed eigenvalues v.s. the mesh sizes are plotted at several critical points of the Brillouin zone, namely, the points of high symmetry: Γ, X, and M, as first shown in Figure 3.1. These points are of great importance as the sites of the optimal eigenvalues, and will be discussed in the next subsection 3.1.4 when band structures are computed. The convergence of the first 20 eigenvalues is plotted; using the convergence rate as

defined below in (3.1.13), it is observed to be $r \approx 2 = 2p$, where $p = 1$ is the order of the interpolation polynomials for the finite element basis functions. This convergence rate is consistent with the value reported in the literature for the Galerkin finite element method [10, 15].

$$r = \log_{h'/h} \frac{e_{h'}}{e_h}. \tag{3.1.13}$$

Eigenvalue convergence on inhomogeneous domain

Next we examine the convergence of the eigenvalues in an inhomogeneous domain. The computation domain (one primitive cell of the photonic crystal) consists of a column of radius $0.2a$ with dielectric material GaAs ($\varepsilon_H = 11.4$) in vacuum ($\varepsilon_L = 1$). To ensure that the dielectric functions used in all the examples are the same, the dielectric variable $\boldsymbol{\varepsilon}$ representing the column of said radius is created on a 32×32 uniform mesh, and extrapolated to various finer uniform meshes(Figure 3.10(a),(b), and(c)), or to adaptively refined non-uniform meshes (Figure 3.10(d),(e), and(f)) using the procedure described in section 3.1.3. By this approach, the resolution of the circular dielectric is determined by the coarsest mesh. Figure 3.10 demonstrates the refinement history for the uniform mesh extrapolation and nonuniform mesh adaptivity.

Due to the lack of an analytical solution, the solution from the finest mesh ($n = 256$) is considered as the "truth" solution (not shown in Figure 3.10). The errors of the jth eigenvalue λ_h^j on a uniform mesh and $\lambda_{h_{equiv}}^j$ on a nonuniform mesh are defined slightly differently as,

$$e_h^j = \|\lambda_h^j - \lambda_{h=a/256}^j\| / \|\lambda_{h=a/256}^j\|, \tag{3.1.14a}$$

$$e_{h_{equiv}}^j = \|\lambda_{h_{equiv}}^j - \lambda_{h=a/256}^j\| / \|\lambda_{h=a/256}^j\|. \tag{3.1.14b}$$

The first 20 eigenvalues of the TE polarization have been computed, and their errors versus the grid sizes h (or h_{equiv} for nonuniform mesh) are plotted in Figure 3.11. The results in the uniform meshes are consistent with the previous observations from the homogeneous domain case, i.e., an approximate convergence rate of 2. In the non-uniform meshes, the convergence rate can be as high

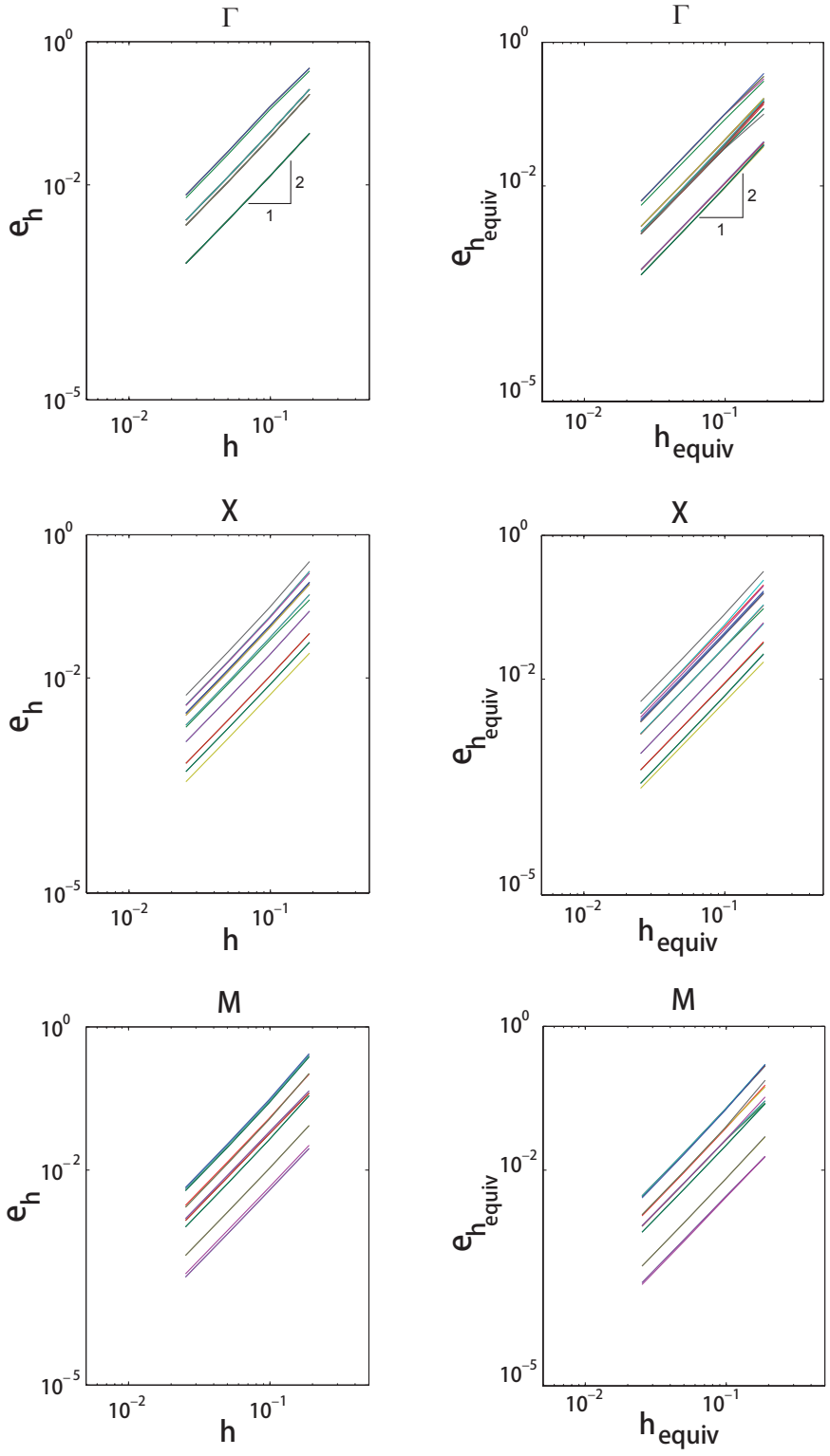

(a) Uniform mesh

(b) Non-uniform mesh

Figure 3.9: Eigenvalue convergence on homogeneous domain. Γ, X, and M indicate the vertices of the irreducible Brillouin zone. Each line represents the convergence of one of the first 20 eigenvalues, while the lowest line corresponds to the smallest eigenvalue.

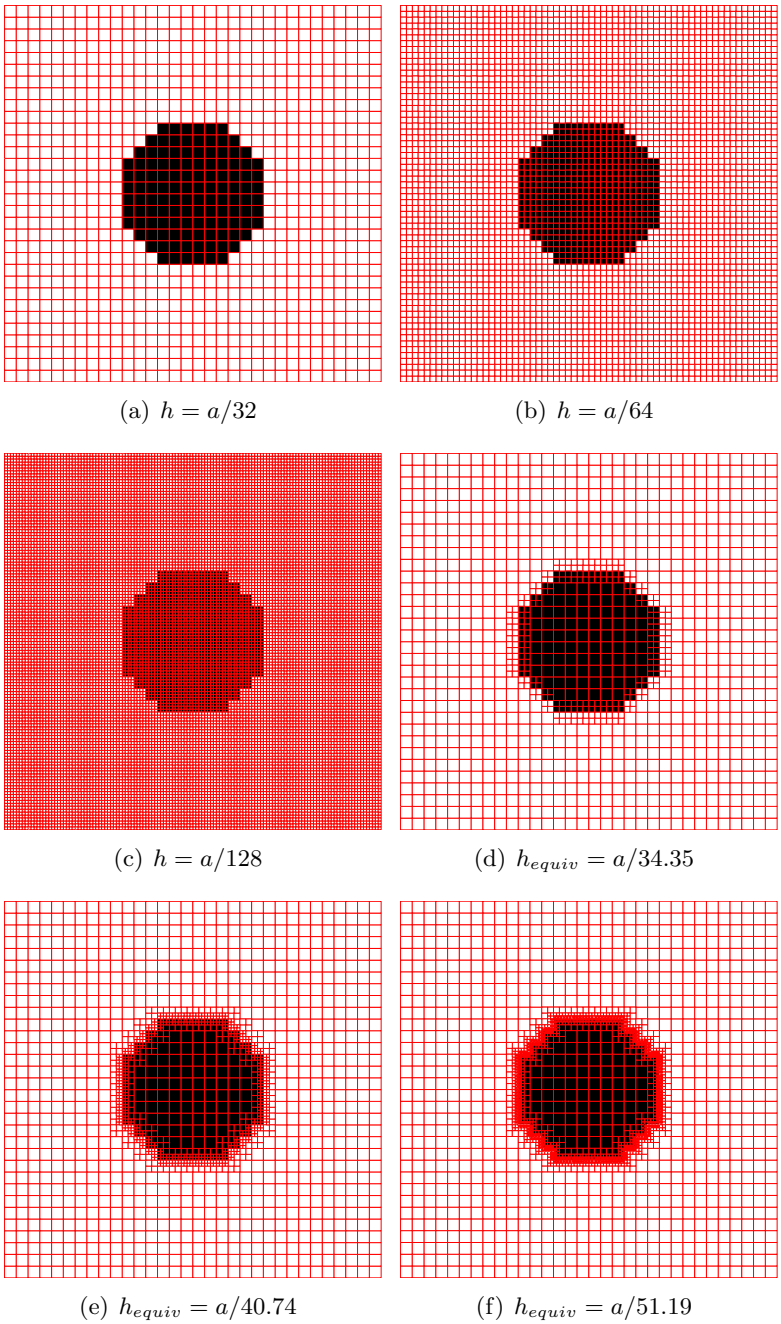

(a) $h = a/32$ (b) $h = a/64$

(c) $h = a/128$ (d) $h_{equiv} = a/34.35$

(e) $h_{equiv} = a/40.74$ (f) $h_{equiv} = a/51.19$

Figure 3.10: Computation meshes used on inhomogeneous domain. Meshes (a), (b), and (c) are used to study eigenvalue convergence on uniform meshes. Meshes (d), (e), and (f) are used to study the convergence on adaptive meshes.

as $r \approx 9$. Additionally, the error plots corresponding to the non-uniform meshes indicate that while fewer DOFs are required, smaller errors can be achieved. This proves that the adaptive mesh refinement procedure is both efficient and effective.

Band structure

Having analyzed the accuracy and convergence of the eigenvalue computation, we also examined the effect of discretization on the band structure, namely, how the numbers of n_k determines the calculated eigenvalue band structures. The eigenvalue band structure of a photonic crystal is typically plotted as the eigenmodes $\lambda_i(\boldsymbol{k}), i = 1, 2, ...,$ (vertical axis) versus the wave vector $\boldsymbol{k}$ (horizontal axis). For two- and three-dimensional photonic crystals, the discrete boundary of the irreducible Brillouin zone is mapped onto the horizontal axis. A band gap is identified as the void between the lower band and higher band at a given wave vector. When the void expands to cover all the wave vectors of the irreducible Brillouin zone, i.e., the entire horizontal axis, an absolute band gap arises, such as the demonstrations in Figures 3.12 and 3.13. While the eigenvalue bands become smoother and more defined as the discretization resolution of the irreducible Brillouin zone boundary increases, the resulting band gap (in blue shade) size is not affected, since the optima of the eigenvalues often occur at the important symmetry points – vertices of $\partial\mathcal{B}$, Γ, X, and M.

3.2 Band Structure of Three-dimensional Photonic Crystal Fiber

3.2.1 Governing equations

To describe the three-dimensional structure of the photonic crystal fiber, we start with the two-dimensional photonic crystal we are familiar with, a photonic crystal with translational symmetry over two of its axes ($xy-$ plane), and homogeneous along the third axis ($z-$axis). In contrast with the strictly periodic two-dimensional case, where the propagation is limited to the $xy-$ plane (i.e., $\boldsymbol{k} = \boldsymbol{k}_{xy} + k_z$, and $k_z = 0$), the propagation direction of electromagnetic

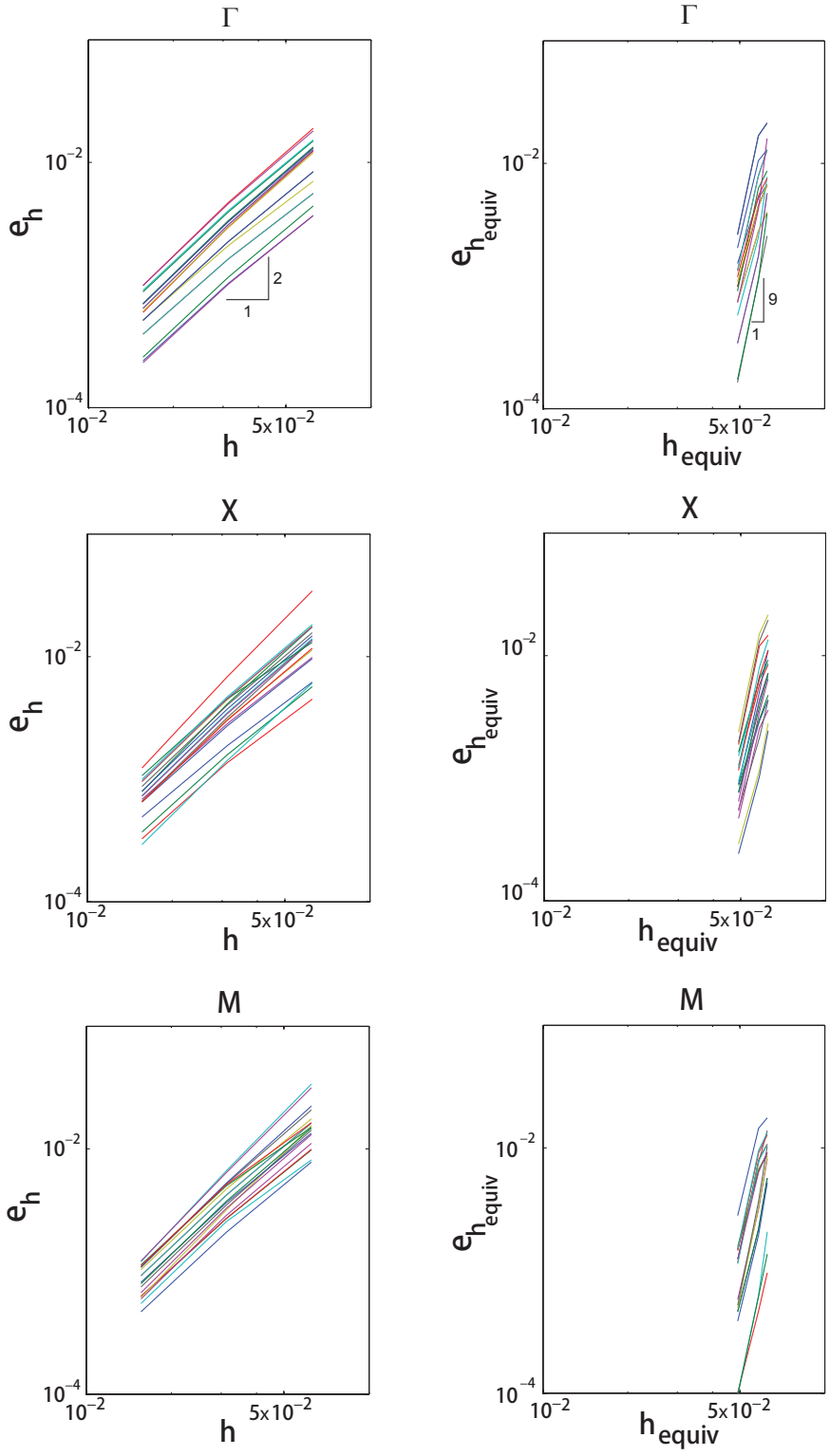

(a) Uniform mesh

(b) Non-uniform mesh

Figure 3.11: Eigenvalue convergence on inhomogeneous domains. Γ, X, and M indicate the vertices of the irreducible Brillouin zone. Each line represents the convergence of one of the first 20 eigenvalues, while the lowest line corresponds to the smallest eigenvalue.

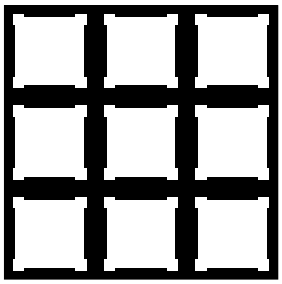

(a) Geometry: connected dielectric veins.

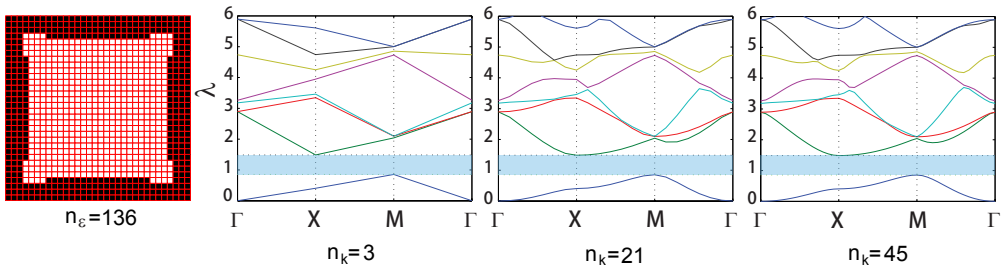

(b) Uniform mesh with $h = a/32$

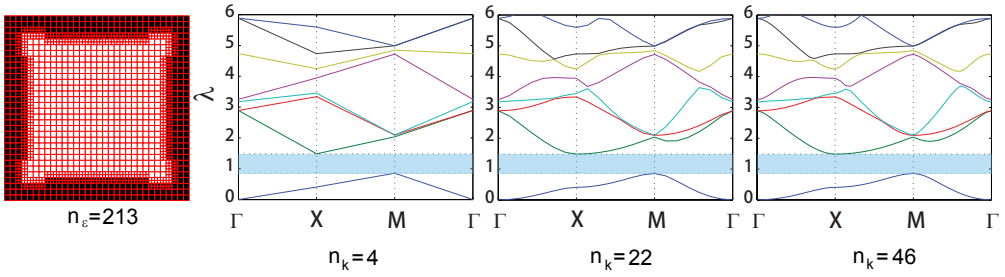

(c) Non-uniform mesh with $h_{\min} = a/64$

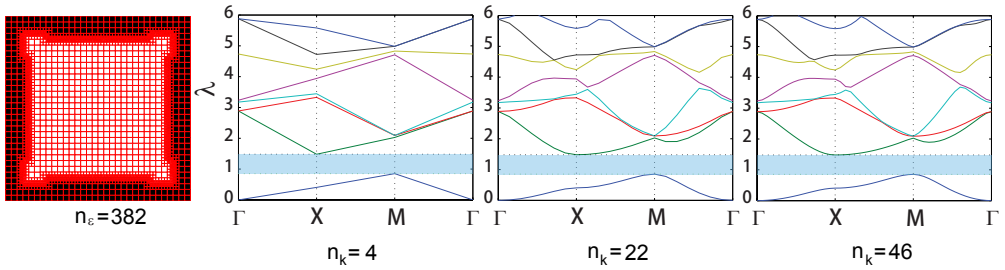

(d) Non-uniform mesh with $h_{\min} = a/128$

Figure 3.12: TE Band diagrams of a connected dielectric vein structure on a square lattice. Successively refined computation meshes (increasing n_ϵ) and higher discretization resolution of the irreducible Brillouin zone boundary (increasing n_k) are used for band structure calculation.

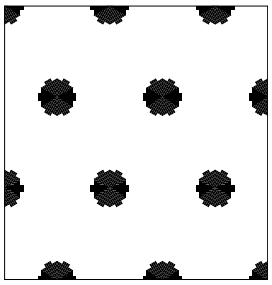

(a) Geometry: isolated dielectric columns.

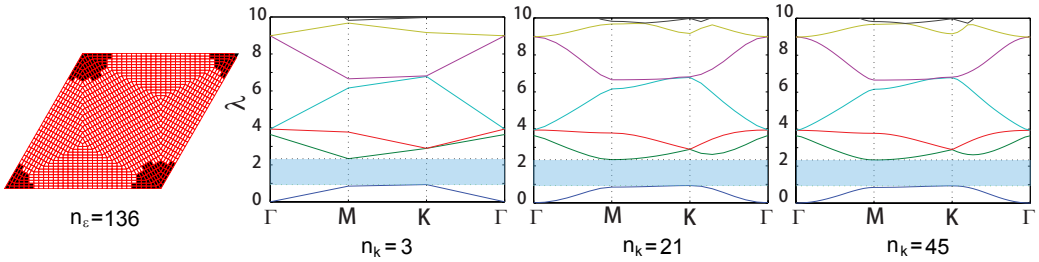

(b) Uniform mesh with $h = a/32$

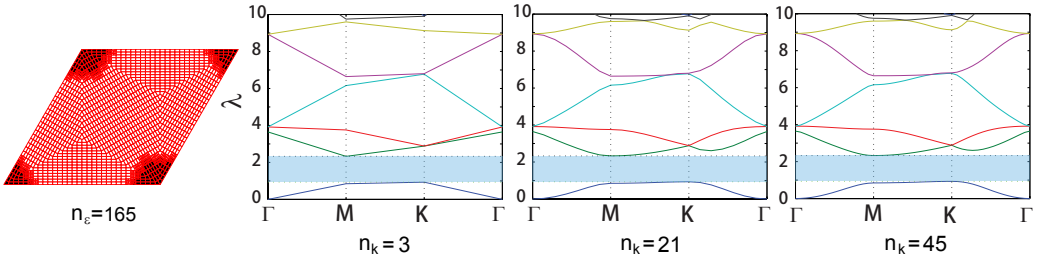

(c) Non-uniform mesh with $h_{\min} = a/64$

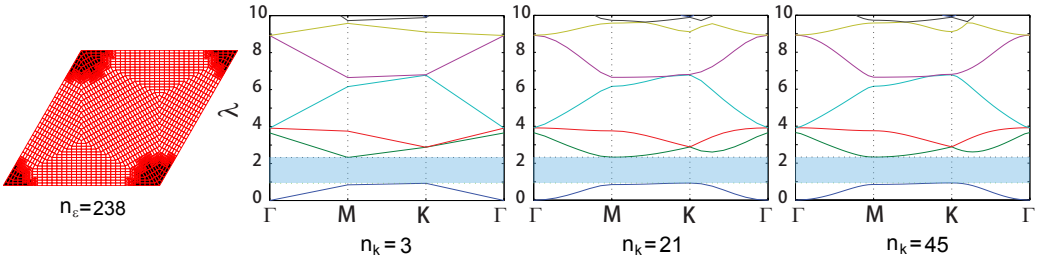

(d) Non-uniform mesh with $h_{\min} = a/128$

Figure 3.13: TM Band diagrams of an isolated dielectric column structures on a hexagonal lattice. Successively refined computation meshes (increasing n_ϵ) and higher discretization resolution of the irreducible Brillouin zone boundary (increasing n_k) are used for band structure calculation.

waves in a three-dimensional fiber is along the fiber axis (taken to be the z-axis), i.e., $\boldsymbol{k}_{xy} = 0$. Next, the translational symmetry over the xy-plane is disrupted by introducing a defect known as *core*; the surrounding region is called photonic crystal *cladding*. In the most general case, the structure is described by a dielectric function $\varepsilon(x, y, z) = \varepsilon^{CL}(x, y, z) + \varepsilon^{CO}(x, y, z)$; $\varepsilon(x, y, z), \varepsilon^{CL}(x, y, z)$ and $\varepsilon(x, y, z)$ are all periodic with period $a_z (a_z \to 0$ in the case of constant cross-section); the cladding dielectric function $\varepsilon^{CL}(x, y, z)$ is periodic in xy (or homogeneous in a conventional fiber). Supported by numerous numerical calculations [38], exponentially localized index-guided modes can be obtained if the refractive index (or dielectric constant) is increased in the core, i.e., $\varepsilon^{CO}(x, y, z)$ is non-negative.

We start with the master equation for macroscopic Maxwell equations (3.1a). Because the fiber is translationally symmetric along the z-axis, k_z is conserved across the dielectric interface (and is commonly referred in the waveguide literature as the propagation constant, and denoted by β). The field variable can be written in Bloch form

$$\boldsymbol{H}(\boldsymbol{r}) = \boldsymbol{H}(x, y)e^{i\beta z}. \tag{3.2.1}$$

Therefore, equation (3.1a) can be reduced to

$$(\nabla_\perp + i\beta \boldsymbol{e}_z) \times \left(\varepsilon^{-1}(\nabla_\perp + i\beta \boldsymbol{e}_z) \times \boldsymbol{H}(x, y)\right) = \lambda \boldsymbol{H}(x, y), \quad \text{in } \Omega_s, \tag{3.2.2}$$

where $\nabla_\perp = \frac{\partial}{\partial x}\hat{\boldsymbol{x}} + \frac{\partial}{\partial y}\hat{\boldsymbol{y}}$ is the transverse gradient operator. Computation domain is the super cell Ω_s, which expands to the fiber cross-section and includes multiple primitive unit cells. If we further split $\boldsymbol{H}(x, y)$ into a transverse part $\boldsymbol{H}_\perp(x, y) = H_x(x, y)\hat{\boldsymbol{x}} + H_y(x, y)\hat{\boldsymbol{y}}$ and a longitudinal part $\boldsymbol{H}_\parallel(x, y) = H_z(x, y)\hat{\boldsymbol{z}}$, then

$$\boldsymbol{H}(x, y) = \boldsymbol{H}_\perp(x, y) + H_z(x, y)\hat{\boldsymbol{z}}. \tag{3.2.3}$$

Substituting it into (3.2.2), we obtain

$$\begin{aligned} \nabla_\perp \times \left(\varepsilon^{-1}\nabla_\perp \times \boldsymbol{H}_\perp\right) + \beta^2\varepsilon^{-1}\boldsymbol{H}_\perp + i\beta\varepsilon^{-1}\nabla_\perp H_z &= (\omega/c)^2\boldsymbol{H}_\perp, \\ i\beta\nabla_\perp \cdot \varepsilon^{-1}\boldsymbol{H}_\perp - \nabla_\perp \cdot \left(\varepsilon^{-1}\nabla_\perp H_z\right) &= (\omega/c)^2 H_z, \quad \text{in } \Omega_s. \end{aligned} \tag{3.2.4}$$

For notational convenience, we rewrite the system of equations in the following operator form:

$$\mathcal{A}\boldsymbol{u} = \lambda \mathcal{M}\boldsymbol{u}, \qquad \text{in } \Omega_s, \tag{3.2.5}$$

where $\lambda \equiv (\omega/c)^2$, and

$$\mathcal{A}(\varepsilon, \beta) \equiv \begin{bmatrix} \nabla_\perp \times \left(\varepsilon^{-1}\nabla_\perp \times\right) + \beta^2 \varepsilon^{-1} & i\beta\varepsilon^{-1}\nabla_\perp \\ i\beta\nabla_\perp \cdot \varepsilon^{-1} & -\nabla_\perp \cdot \left(\varepsilon^{-1}\nabla_\perp\right) \end{bmatrix}, \qquad \mathcal{M} \equiv I, \qquad \boldsymbol{u} \equiv \begin{bmatrix} \boldsymbol{H}_\perp \\ H_z \end{bmatrix}. \tag{3.2.6}$$

We denote by (u^m, λ^m) the m-th pair of eigenfunction and eigenvalue of (3.1.3) and assume that these eigen pairs are numbered in ascending order: $0 < \lambda^1 \leq \lambda^2 \leq \cdots \leq \lambda^\infty$.

The formulation shown in (3.2.6) is also known as the *resonance problem*. When the third dimension is homogenous as the photonic crystal fiber, the original three-dimensional vectorial problem (3.1) is reduced to a two-dimensional vectorial eigenproblem; comparing with the eigenproblem in section 3.1, the original two-dimensional vectorial problem was reduced to two two-dimensional scalar problems, when the propagation wave vector $\boldsymbol{k}(x, y)$ is limited to the cross section of the two-dimensional photonic crystal structures.

We need to keep our numerical scheme simple enough for the optimization formulation (to be discussed in Chapter 5) yet not oversimplified to result in the loss of accuracy. Essentially, two types of eigenmodes will be sought. The first type relates to the modes in a photonic crystal cladding with perfect translational symmetry, from which the fundamental space filling mode will be calculated. A periodic boundary condition on the primitive unit cell Ω suffices in this case. The second type involves the modes in a disrupted cladding, also known as the photonic crystal fiber, or in the most general case, the waveguide. In this case, we are seeking only the *guided modes*, whose corresponding magnetic field decays exponentially away from the core to zero inside the cladding region within a finite domain, i.e., the super cell Ω_s if it is set large enough. While most boundary conditions would be satisfied in this case, the periodic boundary condition is again chosen for consistency and simplicity.

3.2.2 Discretization

Mixed continuous Galerkin

The most well-known issue with the finite element method for solving three-dimensional electromagnetic eigenproblems is the introduction of *spurious modes* [54], i.e., nonphysical eigenvalues which appear in the computed spectrum polluting the correct, physical eigenvalues. This is believed to attribute to the improper modeling of the discontinuities of the field variables across dielectric boundaries by node elements. Recall that node elements enforce the continuity of the field variables over the entire computation domain. However, Maxwell equations require the continuity of the *tangential* component of the field variables across dielectric boundaries. Tangential vector finite elements, also known as edge elements, need to be introduced to enforce the tangential continuity of the elements. In our optical waveguide problem where the dimensionality is reduced to two due to longitudinal symmetry, the longitudinal component of the field variable is continuous across material boundaries, while the transverse components are discontinuous and the continuity of their tangential components need to be enforced. As a result, the longitudinal field variable $u_z (\in H^1(\Omega))$ is represented by node elements, and the transverse field variable $u_\perp (\in H(curl, \Omega) \equiv \left\{ \boldsymbol{v} \in [L^2(\Omega)]^2 \mid \nabla_\perp \times \boldsymbol{v} \in [L^2(\Omega)]^2 \right\})$ is represented by edge elements to ensure that all the non-zero eigensolutions correspond to valid waveguide modes [37, 22].

The strategy described above is called the mixed formulation, and was first proposed by Kikuchi in [35]. In the same paper, he also pointed out the presence of an infinitely degenerate eigenvalue "0" whose eigenspace lies in the functional space of the field variables. To understand this issue, we can apply the Helmholtz decomposition to split the field variable into curl-free and divergence-free parts:

$$\begin{bmatrix} \boldsymbol{H}_\perp \\ H_z \end{bmatrix} = \underbrace{\begin{bmatrix} \nabla_\perp \varphi \\ i\beta\varphi \end{bmatrix}}_{curl-free} + \underbrace{\begin{bmatrix} \boldsymbol{u}_\perp \\ u_z \end{bmatrix}}_{div-free}. \tag{3.2.7}$$

The curl-free part is non-physical and violates the divergence condition. It also

resides in the null space of the operator $\mathcal{A}$ of (3.2.5). Therefore, an eigen solver which minimizes the Rayleigh quotient will inevitably converge to this null space. It is thus meaningful to include the divergence free constraint to eliminate the non-physical eigensolutions. A mixed formulation based on Lagrange multiplier $p(\in H_0^1(\Omega) \equiv \left\{v \in H^1(\Omega) \mid v \mid_{\partial\Omega} = 0\right\})$ [5, 14] is a typical method to relax such a condition. The modified operators are such that,

$$\mathcal{A}(\varepsilon,\beta) \equiv \begin{bmatrix} \nabla_\perp \times \left(\varepsilon^{-1}\nabla_\perp \times\right) + \beta^2\varepsilon^{-1} & i\beta\varepsilon^{-1}\nabla_\perp & \nabla_\perp \\ i\beta\nabla_\perp \cdot \varepsilon^{-1} & -\nabla_\perp \cdot \left(\varepsilon^{-1}\nabla_\perp\right) & i\beta \\ \nabla_\perp \cdot & i\beta & \mathbf{0} \end{bmatrix}, \; \mathcal{M} \equiv \begin{bmatrix} I & & \\ & I & \\ & & \mathbf{0} \end{bmatrix}, \; \boldsymbol{u} \equiv \begin{bmatrix} \boldsymbol{H}_\perp \\ H_z \\ p \end{bmatrix} \tag{3.2.8}$$

$H^1(\Omega)$ and $H(curl, \Omega)$ conforming basis

We briefly review the two types of interpolation basis functions to be used for the finite element discretization of equation (3.2.8). Throughout our work, we employ isoparametric quadrilateral elements, i.e., the shape functions for geometric mapping from the reference coordinate system (ξ, η) to the (x, y) coordinate system are of the same order as the $H^1(\Omega)$ conforming nodal basis functions.

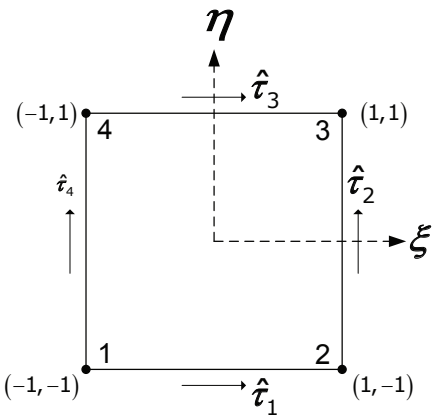

Figure 3.14: Reference quadrilateral element.

Over the reference square element shown in 3.14, recall that the linear $H^1(\Omega)$ conforming basis functions $\hat{\varphi}_i(\xi, \eta),\ i = 1, \ldots, 4$, can be expressed as (illustrated in Figure 3.15)

$$\hat{\varphi}_1 = \frac{1}{4}(1-\xi)(1-\eta), \quad \hat{\varphi}_2 = \frac{1}{4}(1+\xi)(1-\eta), \quad \hat{\varphi}_3 = \frac{1}{4}(1+\xi)(1+\eta), \quad \hat{\boldsymbol{\psi}}_4 = \frac{1}{4}(1-\xi)(1+\eta). \tag{3.2.9}$$

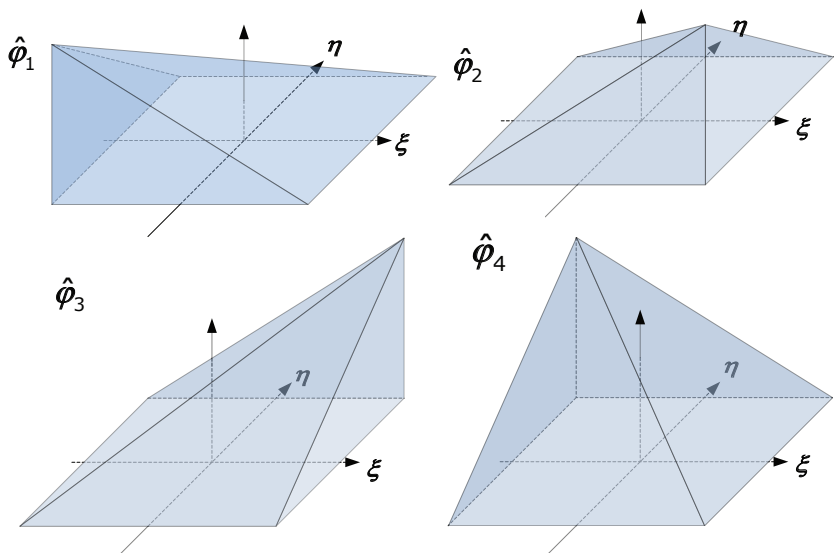

Figure 3.15: $H^1(\Omega)$ conforming basis functions.

The hat denotes a quantity expressed relative to the reference coordinate system (ξ, η). The scalar field variable $\hat{u}_z$ over the element can be interpolated as

$$\hat{u}_z = \sum_{i=1}^{4} u_{zi}\hat{\varphi}_i, \tag{3.2.10}$$

where the scalar coefficients u_{zi} are the unknowns.

Next, the lowest order $H(curl, \Omega)$ conforming basis functions $\hat{\boldsymbol{\psi}}_i(\xi, \eta),\ i = 1, \ldots, 4$, over the reference element can be expressed as

$$\hat{\boldsymbol{\psi}}_1 = \frac{1}{2}(1-\eta)\begin{bmatrix} 1 \\ 0 \end{bmatrix}, \quad \hat{\boldsymbol{\psi}}_2 = \frac{1}{2}(1+\xi)\begin{bmatrix} 0 \\ 1 \end{bmatrix}, \quad \hat{\boldsymbol{\psi}}_3 = \frac{1}{2}(1+\eta)\begin{bmatrix} 1 \\ 0 \end{bmatrix}, \quad \hat{\boldsymbol{\psi}}_4 = \frac{1}{2}(1-\xi)\begin{bmatrix} 0 \\ 1 \end{bmatrix}. \tag{3.2.11}$$

This is illustrated in Figure 3.16.

If the unit tangent vector of an edge i is denoted by $\boldsymbol{\tau}_i$, then these vector basis functions satisfy the requirements $\boldsymbol{\tau}_i \cdot \hat{\boldsymbol{\psi}}_j = \delta_{ij}$, where δ_{ij} is the Kronecker Delta. Therefore, the vector field variable $\hat{\boldsymbol{u}}_\perp$ over the element can be interpolated as

$$\hat{\boldsymbol{u}}_\perp = \begin{bmatrix} \hat{u}_\xi \\ \hat{u}_\eta \end{bmatrix} = \sum_{i=1}^{4} u_{\perp i}\hat{\boldsymbol{\psi}}_i, \tag{3.2.12}$$

where the scalar coefficients $u_{\perp i}$ are the unknowns and are constant on each edge i.

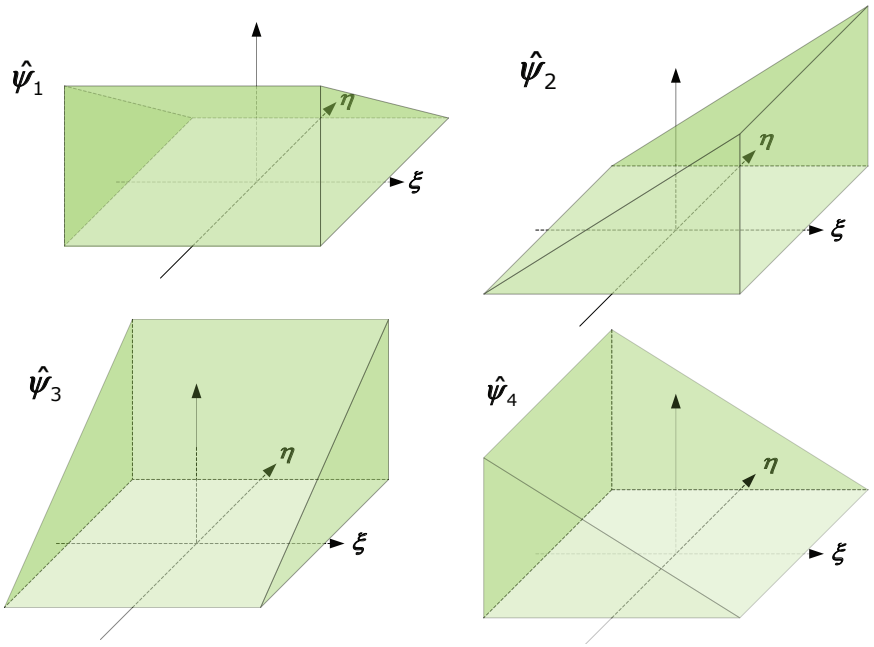

Figure 3.16: $H(curl, \Omega)$ conforming basis functions.

Discretization

We follow the similar procedure described in section 3.1.2 to discretize the infinite dimensional eigenvalue problem. First, we discretize the one-dimensional propagation constant in the range of $[0, \beta_M]$:

$$\mathcal{P}_h = \{\beta_t \in [0, \beta_M], 1 \leq t \leq n_\beta\}\,. \tag{3.2.13}$$

Second, the super cell Ω_s is decomposed into N disjoint subcells $K_i, 1 \leq i \leq N$, such that $\Omega_s = \cup_{i=1}^{N} K_i$, and the shared interface of the two neighboring elements K_i and K_j is denoted by e_{ij}. The dielectric function $\varepsilon(x, y, r)$ takes a uniform value between ε_L and ε_H on each element, where ε_L and ε_H are dielectric constants of a low-index material and a high-index material that make up the cross section of the photonic crystal fiber. That is, $\varepsilon(\boldsymbol{r}) = \varepsilon_j (\in \mathbb{R})$ on K_i, and $\varepsilon_L \leq \varepsilon_j \leq \varepsilon_H$. Instead of the square and hexagonal lattices used in section 3.1, we use the rectangular and hexagonal lattices to avoid the double degeneracy of the fundamental space filling mode [38]. This choice is explained in details where the optimization problem is formulated in Chapter 5. As shown in Figure 3.17, both lattices have 4–fold symmetry. Dielectric variables are defined only on the highlighted cells, with the rest obtained through symmetry.

The symmetry lines are marked by red dashes. The structure of the cross-section can now be completely characterized by the dielectric variable vector for the cladding $\boldsymbol{\varepsilon}^{CL}$, and the vector for the core $\boldsymbol{\varepsilon}^{CO}$, i.e., $\boldsymbol{\varepsilon} = \left[\boldsymbol{\varepsilon}^{CL}; \boldsymbol{\varepsilon}^{CO}\right] = \left[\varepsilon_1^{CL}, \ldots, \varepsilon_{n_{\varepsilon CL}}^{CL}, \varepsilon_1^{CO}, \ldots, \varepsilon_{n_{\varepsilon CO}}^{CO}\right]$. As before, the permissible set is defined as

$$\mathcal{Q}_h \equiv \{\boldsymbol{\varepsilon} : \boldsymbol{\varepsilon} \in [\varepsilon_L, \varepsilon_H]^{n_\varepsilon}\}, \tag{3.2.14}$$

where $n_\varepsilon = n_{\varepsilon CL} + n_{\varepsilon CO}$.

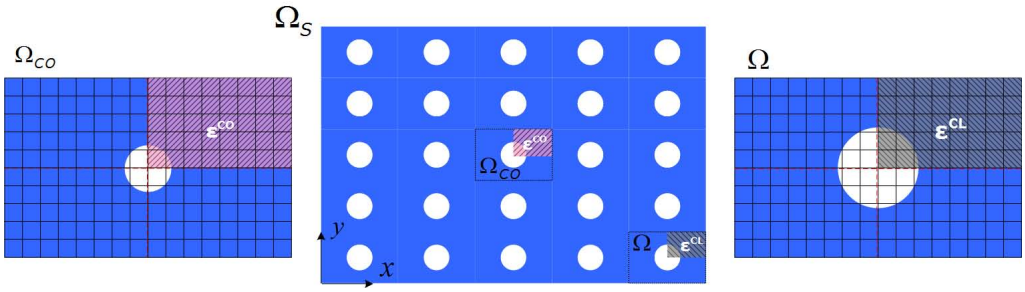

(a) Rectangular lattice

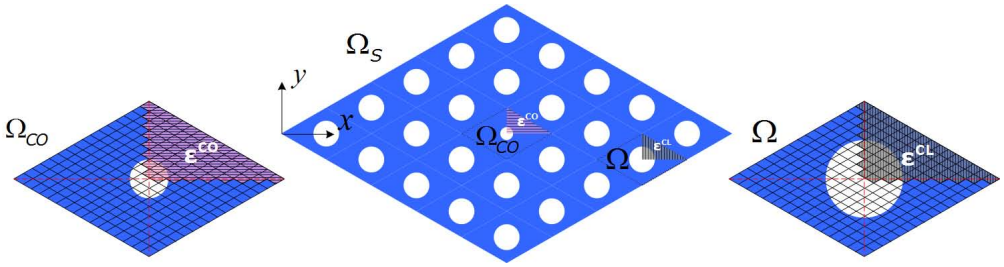

(b) Hexagonal lattice

Figure 3.17: Schematics of the cross-sections of photonic crystal fiber. Left: core region Ω_{CO} made up of one primitive cell; middle: super cell Ω_s; right: one of the primitive cells Ω that make up of the cladding region.

Third, the finite element "truth" approximation spaces of complex valued functions are defined as,

$$X_h \equiv \left\{v \in H^1(\Omega) \mid v|_K \in \mathcal{P}^p(K), \forall K \in \mathcal{T}_h\right\}, \tag{3.2.15a}$$

$$X_h^0 \equiv \left\{v \in H_0^1(\Omega) \mid v|_K \in \mathcal{P}^p(K), \forall K \in \mathcal{T}_h\right\}, \tag{3.2.15b}$$

$$W_h \equiv \left\{v \in H(curl, \Omega) \mid v|_K \in [\mathcal{P}^m(K)]^2, \forall K \in \mathcal{T}_h\right\}. \tag{3.2.15c}$$

$\mathcal{P}^m$ is the space of complex valued polynomials of total degree at most $m = m_{RE} + m_{IM}$ on element K. The weak formulation of the eigenproblem can be stated as follows, find $(\lambda, \boldsymbol{u}_\perp, u_z, p) \in \mathbb{R} \times W_h \times X_h \times X_h^0$, $\forall (\boldsymbol{v}_\perp, v_z, q) \in$

$W_h \times X_h^0 \times X_h^0$, such that

$$\begin{aligned}(\nabla_\perp \times \boldsymbol{v}_\perp, \boldsymbol{\varepsilon}^{-1}\nabla_\perp \times \boldsymbol{u}_\perp) + \beta^2(\boldsymbol{v}_\perp, \boldsymbol{\varepsilon}^{-1}\boldsymbol{u}_\perp) + i\beta(\boldsymbol{v}_\perp, \boldsymbol{\varepsilon}^{-1}\nabla_\perp u_z) + (\boldsymbol{v}_\perp, \nabla_\perp p) &= \lambda(\boldsymbol{v}_\perp, \boldsymbol{u}_\perp),\\ -i\beta(\nabla_\perp v_z, \boldsymbol{\varepsilon}^{-1}\boldsymbol{u}_\perp) + (\nabla_\perp v_z, \varepsilon^{-1}\nabla_\perp u_z) + i\beta(v_z, p) &= \lambda(v_z, u_z),\\ -(\nabla_\perp q, \boldsymbol{u}_\perp) + i\beta(q, u_z) &= 0.\end{aligned} \tag{3.2.16}$$

Finally, we obtain the discrete equation

$$A_h(\boldsymbol{\varepsilon}, \beta)u_h^{m_j} = \lambda^{m_j} M_h u_h^{m_j}, \qquad \boldsymbol{\varepsilon} \in \mathcal{Q}_h, \qquad \beta \in \mathcal{P}_h, \tag{3.2.17}$$

where

$$A_h(\boldsymbol{\varepsilon}, \beta) = \begin{pmatrix} A_1(\boldsymbol{\varepsilon}) + \beta^2 A_2(\boldsymbol{\varepsilon}) & i\beta B(\boldsymbol{\varepsilon}) & C \\ -i\beta B(\boldsymbol{\varepsilon})^* & D(\boldsymbol{\varepsilon}) & i\beta M_z \\ -C^* & i\beta M_z & \mathbf{0} \end{pmatrix} \quad M_h = \begin{pmatrix} M_\perp & & \\ & M_z & \\ & & \mathbf{0} \end{pmatrix} \quad u_h = \begin{pmatrix} \boldsymbol{H}_{\perp h} \\ H_{zh} \\ p_h \end{pmatrix}. \tag{3.2.18}$$

We can further rewrite the stiffness matrix in terms of its $\varepsilon-$dependence

$$\begin{aligned} A_h(\boldsymbol{\varepsilon}, \beta) &= A_h(\boldsymbol{\varepsilon}^{CL}, \beta) + A_h(\boldsymbol{\varepsilon}^{CO}, \beta) + A_h(\beta) \\ &= \sum_{i=1}^{n_{\varepsilon CL}} \varepsilon_i^{CL} A_{h,i}(\beta) + \sum_{i=1}^{n_{\varepsilon CO}} \varepsilon_i^{CO} A_{h,n_{\varepsilon CL}+i}(\beta) + A_{h,0}(\beta). \end{aligned} \tag{3.2.19}$$

Mesh refinement

The refinement criteria and the treatment of the hanging nodes are exactly the same as described in section 3.1.3 for two-dimensional photonic crystal. The additional complications arises due to edge elements, i.e., $H(curl)$ conforming bases. In our implementation, the lowest of the $H(curl)$ bases are used, along each one of which the field variables take constant values. This leads to minimal modifications to the algorithm: when a hanging node splits an edge (e_1) into two (e_2 and e_3), the field variables along these two edges e_2 and e_3, each belonging to a different smaller element, and e_1, belonging to the larger neighboring element, should have the same value. Hence, these three edges should be assigned with one single degree of freedom.

3.2.3 Results and discussion

Cladding eigenvalue convergence

We first examined the convergence of the mixed formulation in both homogeneous and inhomogeneous domains, using the model problem where the material is homogeneous with dielectric constant $\varepsilon(\boldsymbol{r}) = 1$ everywhere. The analytical eigenvalue in this case is known to be $\lambda_j = (m\pi)^2 + (n\pi)^2 + \beta^2,\ m, n \in \mathbb{Z}$ on a computation domain $\Omega = [-1, 1]^2$. Note that this is for the perfect cladding case, and the computation domain consists of one primitive unit cell. Quadrilateral meshes of both uniform and non-uniform sizes are considered. Shown in Figure 3.8, the uniform mesh is obtained by splitting a regular $n \times n$ Cartesian grid into a total of n^2 squares, giving an uniform element size of $h = a/n$; The non-uniform mesh is obtained by refining half of the elements of the uniform mesh, giving the smallest element size of $h_{\min} = a/(2n)$. Three different meshes are used in each case, $n = 8, 16, 32$. The errors and convergence rate are defined as before in (3.1.12) and (3.1.13). Shown in Figure 3.18 is the convergence of the first 20 eigenvalues at several propagation constants ($\beta = 0, \pi, 2\pi$). The first observation is that the multiplicity of the eigenvalues are well captured by the uniform mesh, because only a few overlapped lines are visible in Figure 3.18(a); whereas in the nonuniform meshes, the degenerate eigenvalues deviate from each other by small margins. The convergence rate in both cases are also approximated to be $r \approx 2 = 2\min(p, m)$, where p and m are the orders of the polynomials employed for $H^(\Omega)$ and $H(curl; \Omega)$ conforming basis functions.

The convergence of the first 20 eigenvalues in inhomogeneous domain is shown in Figure 3.19, with the same setup as in section 3.1.4, and Figure 3.10. Overall, a very stable convergence rate of $r \approx 2$ is demonstrated through the uniform meshes. In the non-uniform meshes, the convergence rate can be as high as $r \approx 6$ for the lower eigenmodes, and less satisfactory convergence ($r < 2$) for the higher modes, as the higher order eigenfunctions are not as sufficiently resolved.

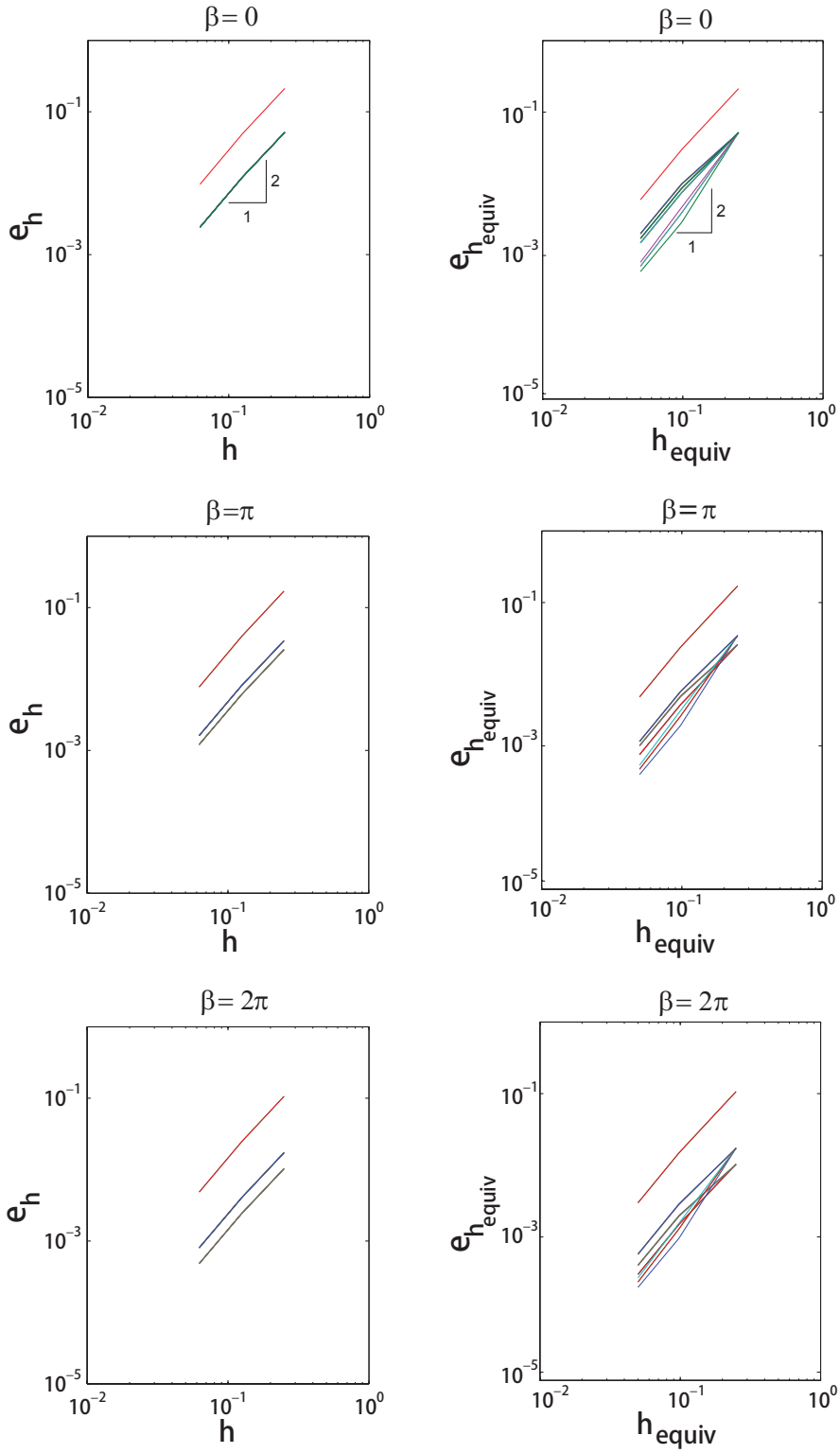

(a) Uniform mesh

(b) Non-uniform mesh

Figure 3.18: Eigenvalue convergence on homogeneous domain at different propagation constants, $\beta = 0, \pi, 2\pi$. Each line represents the convergence of one of the first 20 eigenvalues, while the lowest line corresponds to the smallest eigenvalue.

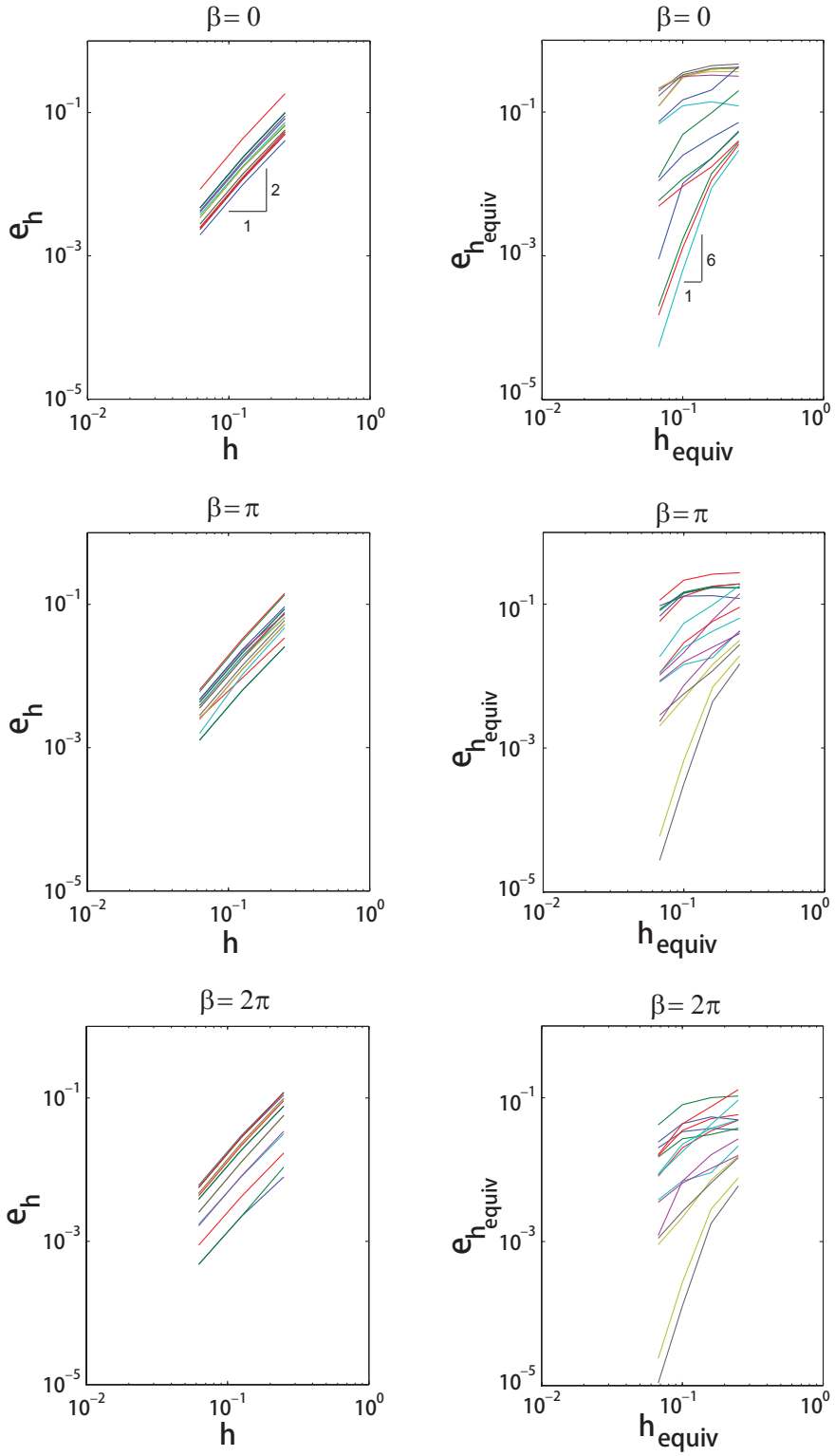

(a) Uniform mesh

(b) Non-uniform mesh

Figure 3.19: Eigenvalue convergence on inhomogeneous domain at different propagation constants, $\beta = 0, \pi, 2\pi$. Each line represents the convergence of one of the first 20 eigenvalues, while the lowest line corresponds to the smallest eigenvalue.

Band structure

To lay the ground work for the optimization problem, we examine in this section the effect of a core being introduced to the otherwise perfect periodic cladding. As introduced in section 1.1.1, a higher ε^{CO} would pull more modes beneath the light line. Hence, we would expect the fundamental eigenmode ($\lambda_h^{WG,1}$) and some higher order modes (say $\lambda_h^{WG,2}$) of the waveguide to be smaller than the fundamental space-filling mode, or light line of the cladding ($\lambda_h^{CL,1}$). Waveguide of both rectangular and rhombic lattices are considered in this section. Two dielectric materials are used to construct the waveguide, epoxy of $\varepsilon_L = 1.5^2 = 2.25$, and silicon carbide of $\varepsilon_H = 2.65^2 = 7.02$. An advantage of using these two materials is that they are both solid at room temperature, therefore it simplifies the issue of non-connectivity. In Figure 3.20(a)(left), a primitive cell Ω of the cladding is constructed as a rectangular lattice (pitch distances $\Lambda_x a = 1.5a$ and $\Lambda_y a = a$) of dielectric material ε_H with cylindrical holes (ε_L) of radius $0.485a$. The primitive cells is used as the building blocks to construct the super cell Ω_s of the waveguide, shown in Figure 3.20(a)(right), not to scale. The core of the waveguide is made up of one Ω with the ε_L hole filled up by ε_H. The cladding consists of two rings of Ω surrounding the core. In Figure 3.20(b), a waveguide set on a rhombic lattice (pitch distance $\Lambda = a$) with elliptical holes of major axis length $0.485a$ and minor axis $0.194a$ is constructed in the same way. In both cases, the dielectric function is computed on a uniform mesh of size $a/20$, and extrapolated to adaptively refined meshes, as shown in the two subplots of Figure 3.21.

The corresponding dispersion relations of the light line and the first two waveguide modes computed on different computation meshes are shown in Figure 3.22. From (i) – (iv), the difference between the waveguide modes and light lines are calculated on successively finer meshes. In all of the four subplots of either rectangular lattice (a) or rhombic lattice (b), the differences between the light line and the fundamental waveguide mode, $\lambda_h^{CL,1} - \lambda_h^{WG,1}$, asymptotically approach zero from a positive value as the frequency decreases (or as the wavelength increases). The positivity of the difference for all $\beta \geq 0$ indicates that the subtrahend is a guided mode, and its asymptocity makes the subtrahend also a

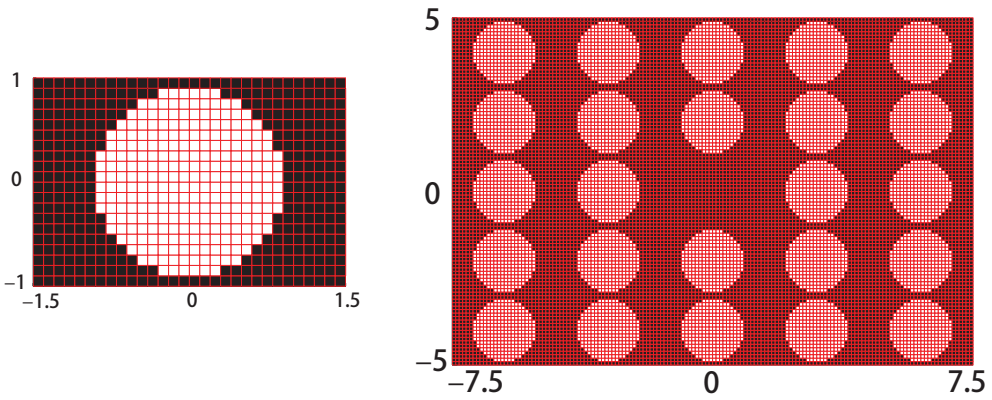

(a) Rectangular lattice

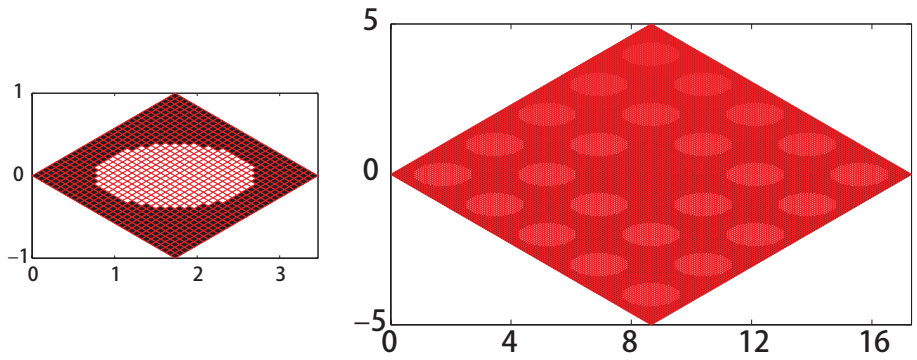

(b) Rhombic lattice

Figure 3.20: Computation meshes for primitive unit cell Ω of cladding (left), and super cell Ω_s of the waveguide (right). The core is formed by removing one ε_L hole and filling it with the ε_H. The cladding consists of two rings of primitive unit cells.

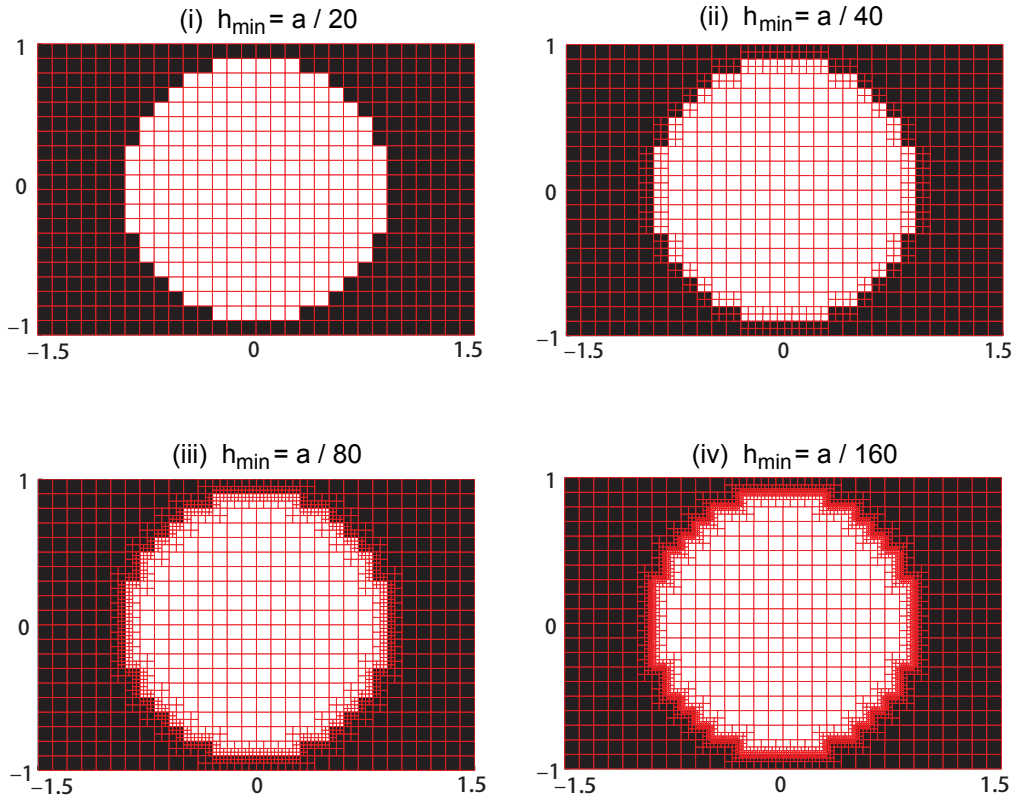

(a) Rectangular lattice

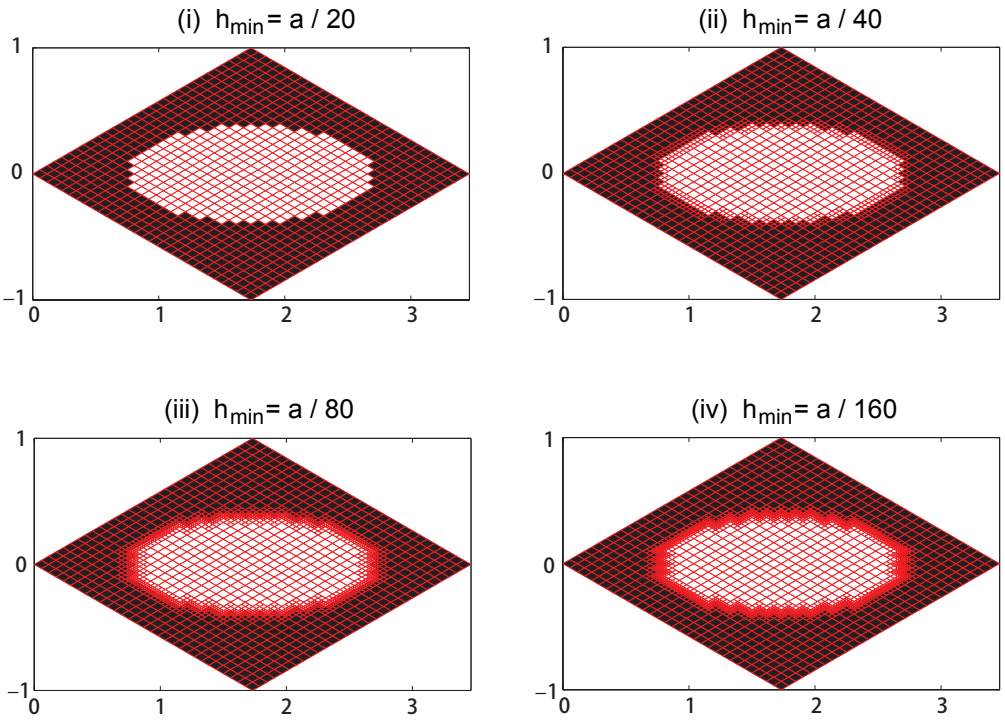

(b) Rhombic lattice

Figure 3.21: Dielectric function is first defined on the coarsest uniform mesh (i), and extrapolated adaptively to finer meshes sequentially (ii) – (iv).

cut-off free mode. However, the differences between the light line and the second waveguide mode, $\lambda_h^{CL,1} - \lambda_h^{WG,2}$, only show nonnegative values for propagation constants $\beta > \beta_c$ (e.g., in Figure 3.22(a), the intersection with the horizontal axis is around $\beta_c a/2\pi = 0.5$). This guided mode is known as a cut-off guided mode. Lee et al have proposed conditions for which these cut-off free and cut-off guided modes would arise [39]. Also shown in the same figure, the guidedness and the cut-off properties of the waveguide modes are not affected by the resolutions of the computation meshes.

3.3 Conclusions

This chapter focused on the numerical solutions to the macroscopic Maxwell equations in the form of Hermitian eigenvalue problems. The numerical recipe chosen for this task is the finite element method, which surpasses others in performance due to its convenient geometrical representation, parameter affinity, and flexible mesh adaptivity.

Two variations based on different physical problems are considered. The first type, two dimensional photonic crystal fiber, describes a dielectric structure that is discretely periodic in the xy-plane, and invariant in the z-axis. The second type, the photonic crystal fiber, is constructed by introducing perturbations across the xy-plane to the perfectly periodic 2D photonic crystal of the first type. This can also be treated as a two-dimensional structure due to its homogeneity along the z-axis.

The governing equation of the two-dimensional photonic crystal can be simplified to two separate scalar equations depending on the polarization of the electromagnetic waves propagating in the xy-plane: transverse electric, or transverse magnetic. These two Laplace-like scalar eigenvalue equations can be discretized by standard finite element method using nodal basis functions for shape and field variable interpolations. The governing equation of the photonic crystal fiber has additional complexity as the propagation direction is along the z-axis, and therefore no advantage can be taken of the polarization. In addition, the special mixed method between edge basis and nodal basis was used for the finite

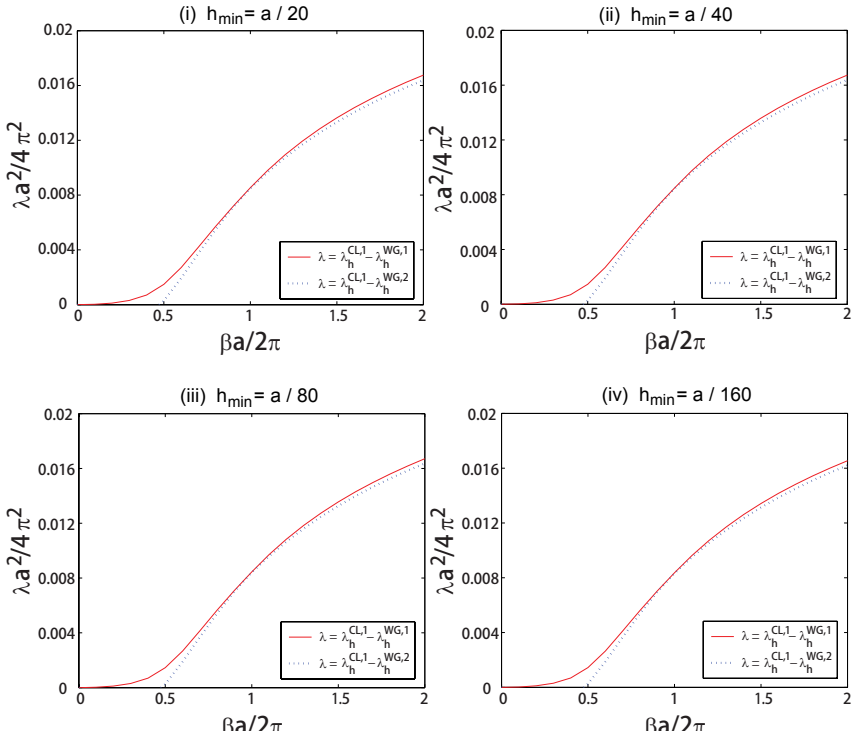

(a) Rectangular lattice

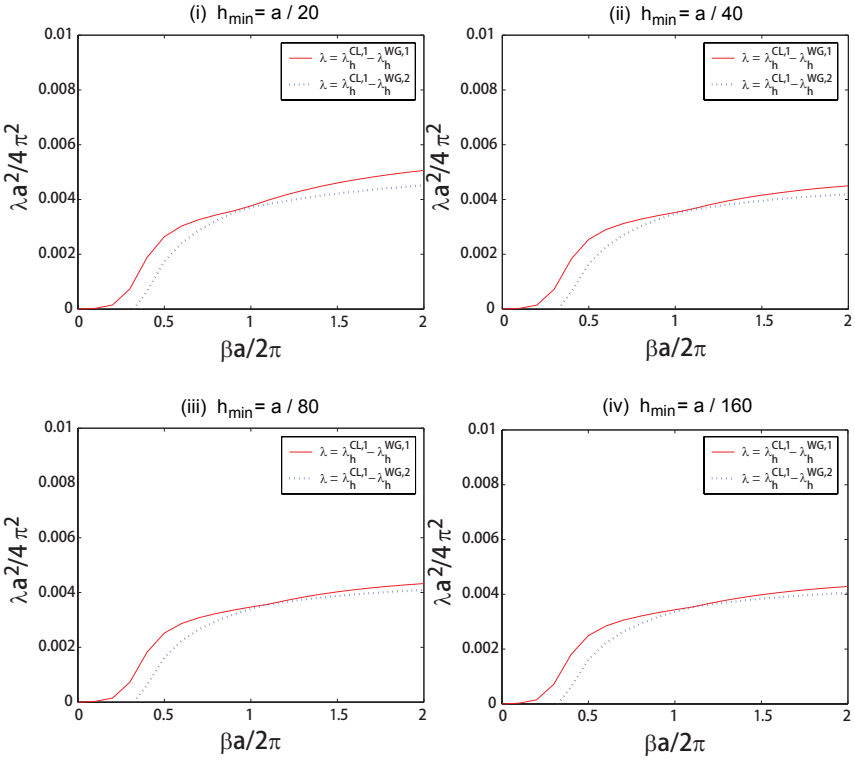

(b) Rhombic lattice

Figure 3.22: Dispersion relation of structures corresponding to those shown in Figures 3.20 and 3.21 on the coarsest uniform mesh (i), and to finer meshes sequentially (ii) – (iv).

element approximation. In either case, we end up with a generalized eigenvalue problem that can be solved by various standard eigen solvers; "eigs" from MATLAB® is our solver of choice throughout this thesis.

Mesh adaptivity has also been introduced and incorporated to discretize the computation domain non-uniformly and represent the material property more efficiently.

Finally, we examined the convergence rate of the numerical methods on both uniform and non-uniform meshes, homogeneous and inhomogeneous domains of various lattices. A consistent convergence rate of $r \approx 2$ has been obtained for the eigenmodes in the uniform meshes. In the non-uniform meshes, the convergence rate can be as high as $r \approx 9$ for the lower eigenmodes. These validated results laid the ground work for the optimization problems in the next two chapters.